A global screen for assembly state changes of the mitotic proteome by SEC-SWATH-MS

Moritz Heusel[1,5], Max Frank[1], Mario Köhler[2], Sabine Amon[1], Fabian Frommelt[1], George Rosenberger[1], Isabell Bludau[1], Simran Aulakh[1], Monika I. Linder[2],Yansheng Liu[3], Ben C. Collins[4], Matthias Gstaiger[1], Ulrike Kutay[2,*], Ruedi Aebersold[1,6,*]ℓ.

1 Institute of Molecular Systems Biology, Department of Biology, ETH Zurich, Zurich, Switzerland.

2 Institute of Biochemistry, Department of Biology, ETH Zurich, Zurich, Switzerland.

3 Department of Pharmacology, Yale University School of Medicine, New Haven, CT 06520, USA

4 School of Biological Sciences, Queen's University of Belfast, UK

5 Division of Infection Medicine (BMC), Department of Clinical Sciences, Lund University, Lund, Sweden

6 Faculty of Science, University of Zurich, Zurich, Switzerland.

ℓ Corresponding author & Lead contact

* Senior authors

Summary

Living systems integrate biochemical reactions that determine the functional state of each cell. Reactions are primarily mediated by proteins that have in systematic studies been treated as independent entities, disregarding their higher level organization into complexes which affects their activity and/or function and is thus of great interest for biological research. Here, we describe the implementation of an integrated technique to quantify cell state-specific changes in the physical arrangement of protein complexes, concurrently for thousands of proteins and hundreds of complexes. Applying this technique for comparison of human cells in interphase and mitosis, we provide a systematic overview of mitotic proteome reorganization. The results recall key hallmarks of mitotic complex remodeling and discover new events, such as a new model of nuclear pore complex disassembly, validated by orthogonal methods. To support the interpretation of quantitative SEC-SWATH-MS datasets, we extend the software *CCprofiler* and provide an interactive exploration tool, *SECexplorer-cc*.

Highlights

- Quantification of proteome assembly state changes using SEC-SWATH-MS
- Systems-wide analysis of assembly state changes in the mitotic proteome
- Discovery and validation of a novel mitotic disassembly intermediate of the nuclear pore complex
- Higher sensitivity and information content compared to thermostability-based approaches for global measurement of proteome states
- *SECexplorer-cc*, an online platform to browse results and investigate proteins newly implicated in cell division

Introduction

Living systems are characterized by a large number of biochemical functions that are tightly interconnected and coordinated (Hartwell et al., 1999; Ideker et al., 2001). Classical biochemical analyses have led to the association of many biochemical functions with proteins and protein complexes. The function of proteins and protein complexes depends on a defined 3D structure of individual proteins, as well as the composition and specific steric arrangement of proteins into protein-protein complexes. Detailed studies on tetrameric hemoglobin have shown that changes in the composition, arrangement or structure of the complex changes its activity (Pauling 1949), a seminal finding that has since become one of the hallmarks of molecular biology. Whereas much of our biochemical understanding is based on in-depth studies of specific complexes, these are time consuming and more importantly, disregard interactions and coordination between different complexes.

Driven primarily by genomics, life science research has been transformed by high throughput, data-driven approaches. Proteomics is the embodiment of this approach for proteins. To date, most proteomic studies have been carried out by *bottom up proteomics*, where proteins are denatured and cleaved into peptides which are then analyzed by mass spectrometry. Whereas this technology has reached a high level of maturity, information about the structure, the composition and steric arrangement of components in a complex are lost. Therefore, for the most part, proteomics has treated proteins as unstructured biopolymers, disregarding structure and organization into complexes as an important layer of function and control.

Recently, several techniques have been proposed that attempt to extend the large scale analysis of proteins towards the detection of conformational changes between different states ((Becher et al., 2018; Dai et al., 2018; Leuenberger et al., 2017; Liu and Fitzgerald, 2016; Schopper et al., 2017; Tan et al., 2018), towards the organization of proteins into complexes (Heusel et al., 2019; Kristensen et al., 2012; Scott et al., 2017; Wan et al., 2015) and towards assigning protein subcellular localization (Dunkley et al., 2004; Foster et al., 2006). Conformational changes of proteins have been detected by using changes in physico-chemical properties including thermostability ((Becher et al., 2018; Dai et al., 2018; Tan et al., 2018)), stability towards denaturing conditions (Xu et al., 2014) or altered protease susceptibility (Leuenberger et al., 2017; Liu and Fitzgerald, 2016; Schopper et al., 2017) as proxy. Inference of complex composition and subcellular localization has been based on chromatographic fractionation, typically by size exclusion chromatography (SEC), of native complexes (Kristensen et al., 2012; Larance et al., 2016; Liu et al., 2008) and subcellular fractions (Dunkley et al., 2004; Foster et al., 2006; Itzhak et al., 2016), followed by the mass spectrometric analysis of the resulting fractions. Pioneering, comparative analyses of co-

58 fractionation patterns of native complexes have revealed extensive re-organization of the
59 modular proteome across metazoans (Wan et al., 2015) and following induction of apoptosis
60 (Scott et al., 2017). However, the co-fractionation approach has been beset by limited SEC
61 resolution, and limitations inherent in data dependent analysis (DDA) mass spectrometry, the
62 method almost universally used in co-fractionation studies. These include limited proteomic
63 depth and accuracy of quantification and stochastic peptide sampling (Aebersold and Mann,
64 2016). Collectively, these limitations resulted in the need for multidimensional separation to
65 assign proteins to specific complexes and, for the most part, unknown error levels of complex
66 assignments (Kristensen et al., 2012; Scott et al., 2017; Stacey et al., 2017; Wan et al., 2015).
67 Recently, we demonstrated increased selectivity and overall performance in co-fractionation-
68 based profiling of cellular complexes using a workflow that is based on single dimension
69 fractionation by high resolution size exclusion chromatography, quantitative measurement of
70 polypeptide elution profiles by SWATH mass spectrometry, an instance of data independent
71 acquisition (DIA)(Gillet et al., 2012, 2016) and the introduction of a complex-centric data
72 analysis strategy (Heusel, Bludau et al., 2019). We also described a software tool *CCprofiler*,
73 that implements a complex-centric strategy to infer protein complexes and uses a target-decoy
74 model to assign a probability to each complex (Heusel, Bludau et al., 2019).

75 Here, we apply SEC-SWATH-MS to detect rearrangements in the modular proteome in HeLa
76 CCL2 cells in two cell cycle states, the interphase and prometaphase. We developed a
77 quantification module for the *CCprofiler* that supports the differential, quantitative analysis of
78 thousands of proteins and their association with complexes. We benchmark the
79 reproducibility of the integrated wet lab/computational method and compare its performance
80 to state-of-the art thermostability-based methods (Becher et al., 2018; Dai et al., 2018). We
81 validate the method by showing that it recapitulates known complex remodeling events
82 between the different states tested. We discover and validate by orthogonal methods a new
83 model of nuclear pore complex disassembly, thus demonstrating the potential of the method
84 to discover new biology. To support additional exploration of the present dataset and future
85 differential SEC-SWATH-MS datasets we provide an online tool, *SECexplorer-cc*.

86 We expect that the parallel quantification of abundance and compositional changes of
87 hundreds of protein complexes will significantly advance our understanding of biochemical
88 mechanisms and processes.

Results

Generation of a SEC-SWATH-MS dataset for the detection of changes in the organization of the mitotic proteome

As basis for our study into mitotic changes in the organization of the proteome, we applied the previously described SEC-SWATH-MS workflow, in conjunction with targeted analysis (Heusel, Bludau et al., 2019) in triplicate to cells synchronized in either cell cycle state as illustrated in **Figure 1A.** Mild cellular extracts containing native proteins and protein complexes were fractionated by high resolution SEC and the proteins in each fraction were digested and quantitatively profiled across the chromatographic fractions by SWATH mass spectrometry (Collins et al., 2017; Gillet et al., 2012; Röst et al., 2014). The samples tested were Hela CCL2 cells synchronized in interphase or mitosis. We inferred changes in complex composition and quantity from the resulting protein apparent size distribution patterns. The mitotic arrest of the respective synchronized cell populations was documented by microscopic assessment of cell shape and the detection of mitosis-specific electrophoretic mobility shifts of hyper-phosphorylated Nup53 and Histone H3 phosphorylation (**Supplemental Figure S1 A-C**). For each of the three replicates performed for either condition, 65 consecutive SEC fractions were collected and for each fraction the proteins were digested and analyzed, by SWATH-MS, generating a quantitative dataset consisting of a total of 390 SEC fractions. The resulting dataset was computationally analyzed using the OpenSWATH software suite and a project specific spectral library as prior information (see **Figure 2A** and experimental procedures for details). Overall, the analysis identified 70,445 peptides associated with 5514 proteins at a TRIC target FDR of 5%. Upon SEC-informed filtering as described previously (Heusel, Bludau et al., 2019), 60,891 peptides and 5,044 proteins were quantified with high confidence across the chromatographic fractions and with an overall decoy-estimated protein level false discovery rate of below 0.4% (see methods for details). Per mitotic condition, we quantified 52,718 and 56,553 peptides resulting in 4,438 and 4,798 protein profiles in interphase and mitosis, respectively (**Figure 1B**). The SEC conditions we used resolved proteins and protein complexes ranging from ca. 5 MDa to 10 kDa with a peak capacity to baseline-separate ca. 20 peaks and showed good reproducibility as apparent from UV/Vis spectrometric traces from the respective samples (**Figure 1C**). The large absorbance at 280 nm observed in the low molecular weight range (fractions 63-80) originated from detergents employed for mild lysis, as evidenced by the drop off of protein-level MS intensities beyond fraction F55, in line with the 30 kDa molecular weight cutoff employed for sample workup (**Figure 1D)**. Even though a comparably high resolution SEC method was used, we detected in the range of ca. 1,200 to 2,000 proteins per fraction (**Figure 1D, lower panel**). Whereas most proteins were detected in both conditions, 4,192 (83%) proteins appeared more readily

125 extractable from mitotic cells (**Figure 1B**). This is apparent from the lower cumulative ion
126 intensities across most fractions (**Figure 1D**) and is potentially a consequence of mitotic
127 reorganization including nuclear envelope breakdown. The thus generated set of protein
128 abundance profiles was the basis for the further analyses.

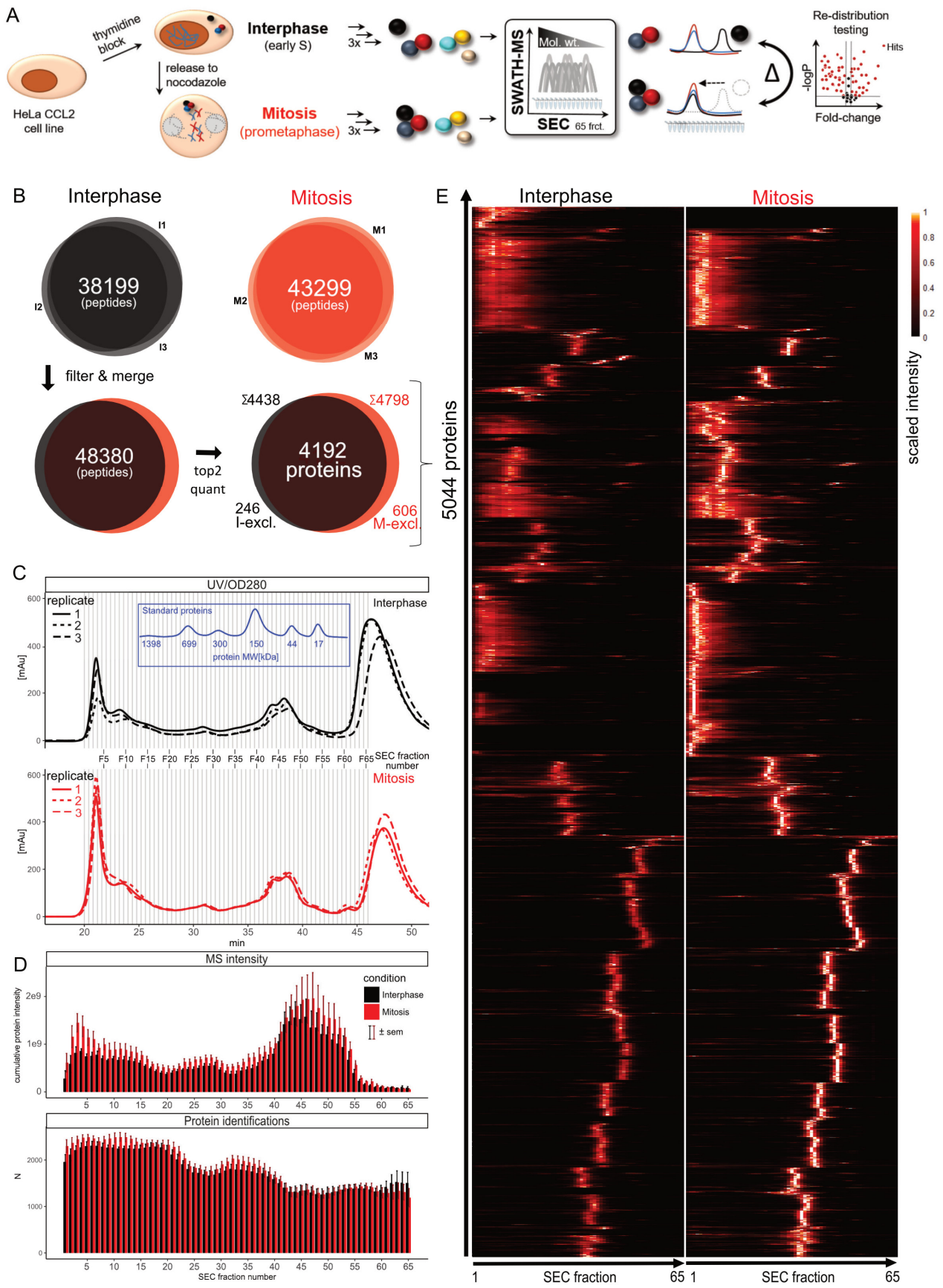

Figure 1: Proteome rearrangement screening by SEC-SWATH-MS: Workflow and dataset properties. **A** Scheme of the SEC-SWATH-MS workflow to screen for mitotic proteome

132 rearrangement. HeLa CCL2 cells were synchronized in interphase or mitosis by chemical treatment,
133 followed by triplicate extraction of complexes by mild lysis, fractionation by size exclusion
134 chromatography and quantitative profiling of eluting proteins. Differential association scoring via
135 *CCprofiler* reveals proteins with altered complex association states between conditions. **B** Peptide
136 identifications across the three experimental repeats and summary per condition on peptide and protein
137 level, giving rise to the dataset overview in panel E. Of the total 5044 observed proteins, most were
138 detected independently in both conditions 4192 (83%). **C** Semi-preparative scale SEC of interphasic
139 and mitotic complex preparations and size reference protein mix monitored by UV/Vis spectroscopy.
140 Elution of standard proteins calibrates the fraction number to apparent molecular weight mapping in
141 the study. **D** Summary of MS-observed protein level intensity and number of confidently identified
142 proteins along the 65 fractions across the repeats and after normalization (See data processing
143 methods). The large absorbance at 280 nm observed in the low molecular weight range originates from
144 detergent employed for mild lysis and does not reflect protein mass that was not sampled in the
145 fractionation scheme, as can be extrapolated from protein-level MS intensities dropping beyond F55,
146 in line with the 30 kDa molecular weight cutoff employed in sample workup. **E** Dataset overview heat
147 map summarizing the data to 5044 conditional protein elution patterns observed. Mean intensities of
148 the top 2 cumulatively highest-intense peptides per protein were summarized from 3 replicate
149 measurements and scaled from 0 to 1 per protein for visualization in heat map. Differential analysis is
150 however performed at the level of individual, protein-specific peptides (See **Figure 2**).

151 Quantification of protein association state changes from SEC-SWATH-MS data

152 The distribution of protein intensities per fraction for either condition provides a bird's eye
153 view of the acquired dataset (**Figure 1E).** To detect proteins that show significant changes
154 with respect to their association with specific protein complexes, we applied a scoring system
155 that quantifies protein mass re-distribution across distinct elution ranges based on two or more
156 proteotypic peptides quantified by SWATH-MS in each peak. The association of proteins
157 with protein complexes was carried out by the *CCprofiler* (Heusel, Bludau et al., 2019) a
158 software tool that implements a complex-centric strategy using prior knowledge of protein
159 complex composition. To detect quantitative changes of protein complex quantity and
160 composition in either cellular state, we added to the *CCprofiler* tool a new module supporting
161 differential quantification. It performs the sequential steps schematically shown in **Figure 2B**.

162 In the first step, signal intensities of SEC-fractions are normalized to a spike-in standard,
163 missing values are imputed using the background signals from neighboring SEC fractions and
164 SEC traces are aligned across experiments (**Figure 2B**, panel 1, for details and tools used see
165 experimental procedures). The result of the first step is a calibrated and refined list of peptides
166 and their respective intensities per fraction.

167 In the second step, the peptide level data are used to detect protein elution peaks along the
168 SEC dimension. This is achieved by selecting a high quality set of peptide traces, by summing

169 peptide intensities across replicates and conditions and by then employing the *CCprofiler*
170 protein-centric analysis module to infer protein elution peaks. An elution peak is derived from
171 the observation of co-eluting peaks of groups of sibling peptides derived from the same parent
172 protein (See **Figure 2B**, step 2. and peak detection summary and example in **Supplemental**
173 **Figure S4A&B**). This analysis resulted in a total of 6,040 elution peaks of 4,515 of the
174 identified proteins. Accordingly, protein-centric analysis successfully detects peptide co-
175 elution peak groups from 90% of the identified proteins and their peptide SEC profile sets,
176 with no high quality elution signal detectable for the remaining proteins at the confidence
177 threshold (q-value < 0.05). The distinctive elution peaks represent unique complex assembly
178 states of the respective proteins. Consistent with previous protein-centric analyses of the
179 proteome of cycling HEK293 cells (Heusel, Bludau et al., 2019), the majority of the observed
180 elution peaks in the present dataset fell into a SEC separation range consistent with the
181 association of the protein with a complex.

182 The distinctive protein elution peaks and their signal intensities computed in step two provide
183 the basis for the third step we term 'differential association testing'. Here, we calculated the
184 log2-transformed abundance of each peptide per replicate for each observed protein elution
185 peak in the six samples, resulting in six quantitative measurements per peptide per elution
186 peak. For each peptide, differential abundance was then tested for each elution event using a t-
187 statistic (**Figure 2B**, step 3. and exemplified for BAF53 in **Supplemental Figure S4B**). To
188 obtain a significance measure of differential abundance of individual protein elution peaks,
189 the median peptide level p-value of all peptides per protein per elution peak were integrated
190 based on a scoring scheme assuming a beta distribution of the respective values, as described
191 (Suomi and Elo, 2017). To generate the final differential protein association map, proteins are
192 represented by the peak with highest fold-change and shifting proteins assigned based on cut-
193 offs along the Benjamini-Hochberg-adjusted p-value (pBHadj score) and absolute SEC-
194 localized fold-change (**Figure 2B**, step 3, right panel).

195 In the last step, differential association to chromatographic peaks detected per protein is then
196 interpreted in the context of reference complexes to infer instances of protein complex
197 remodeling using the complex-centric concept (Heusel, Bludau et al., 2019) (**Figure 2B**, step
198 4 and exemplified in **Supplemental Figure S4C**). The results are finally visualized and
199 browsable via the web tool *SECexplorer-cc* as detailed further below. The extension of the
200 *CCprofiler* toolset by the quantification module thereby supports the automated detection of
201 altered protein association states and inferred protein complex remodeling from SEC-
202 SWATH-MS data and enables the detection of altered protein complexes that are at the core
203 of the present study.

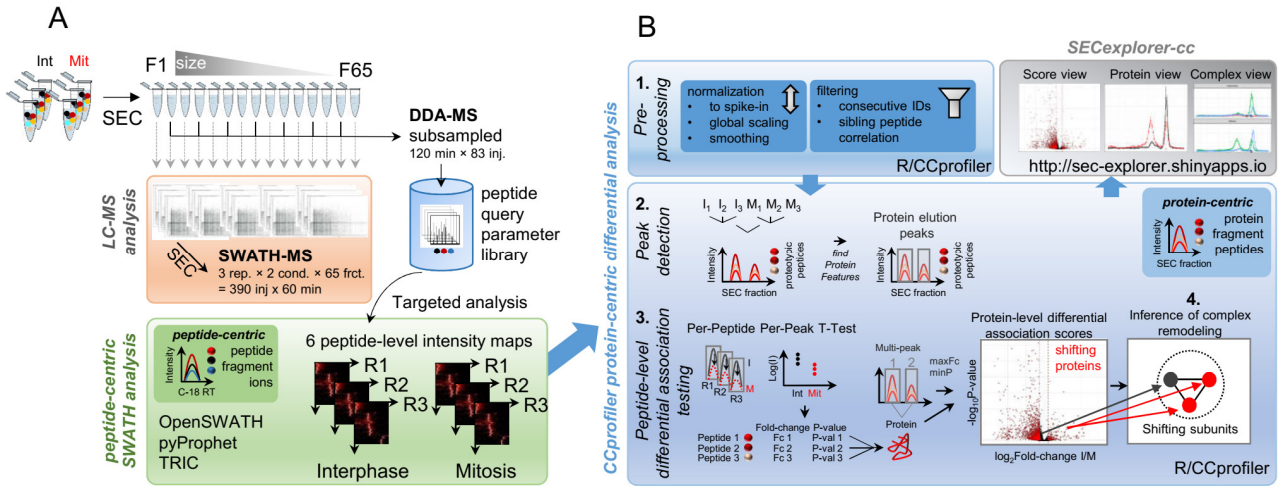

Figure 2: Proteome rearrangement screening by SEC-SWATH-MS: Data acquisition and processing. **A** LC-MS/MS analysis of tryptic peptides generated from 65 fractions per replicate and condition by data-independent acquisition SWATH mass spectrometry (SWATH-MS, n runs = 390). A subsampled set of fractions were subjected to longer 120 min gradient length analysis acquiring data in data-dependent mode to deepen coverage of the sample-specific peptide spectrum and query parameter libraries (DDA-MS, n = 83). Quantitative signals of the targeted peptides is then extracted from the SWATH-MS maps in peptide-centric analysis where peptide analytes are evidenced based on peptide fragment ion signal peak groups along C-18 chromatographic retention time. This produces six peptide-level quantitative matrices as basis for extracting information on protein complex association changes in subsequent differential analysis via *CCprofiler*. **B** Detailed scheme of protein-centric differential analysis of the quantitative peptide-level data via *CCprofiler* involving 1. preprocessing, 2. protein-centric elution peak detection where protein analytes are evidenced based on proteolytic peptide ('protein fragment') signal peak groups along SEC retention time/fraction number and 3. peak-resolved peptide-level statistical scoring to detect differentially associating proteins with shifting mass distribution across SEC fractions. In step 4, from the protein/subunit-level hits protein complex remodeling is inferred in a complex-centric fashion. The results are made available in easily browsable form via *SECexplorer-cc*.

Benchmarking the differential SEC-SWATH-MS workflow and software tool using the mitotic dataset

The application of the method described above to the triplicate data obtained from two cell cycle states indicated substantial rearrangement of the proteome. Specifically, 2,189 SEC elution peaks of 1,793 proteins showed significant changes in abundance (pBHadj score ≤ 0.01, absolute SEC-localized fold-change ≥ 1.5, **Figure 3A**) and 1,626 shifts in the SEC elution range of assembled higher-order complexes. In the following, we further assessed the results at three levels: First, the technical reproducibility of data generation and analysis,

231 second, recall of rearrangements of complexes known to be altered between cell cycle states
232 and third, comparison of the results with those obtained from an orthogonal method from
233 samples in comparable cell cycle states. In particular, we compared the differential SEC-
234 SWATH results with results obtained from the parallel measurement of protein
235 thermostability (Becher et al., 2018; Dai et al., 2018) from which changes in protein
236 complexes were inferred.

237 *Reproducibility*

238 The availability of three replicate SEC-SWATH-MS measurements of either cell cycle state
239 allowed us to assess the reproducibility of the method. Specifically, we evaluated technical
240 cross-replicate variability at the level of i) size exclusion chromatography by the UV/Vis
241 photospectrometric traces, ii) SWATH-MS by peptide and inferred protein identities and their
242 relative abundance and iii) the overall SEC-SWATH-MS workflow by the reproducibility of
243 protein-level SEC chromatograms. SEC fractionation was well-reproducible as is apparent
244 from the UV absorbance profiles (λ = 280 nm) shown in **Figure 1C**. Further, SWATH-MS
245 identified > 80% of detected peptides in all three replicates per cell cycle state and 48,380
246 peptides of 4,192 proteins in both cell cycle states. A total of 5,044 proteins were profiled
247 across both cell cycle states (**Figure 1B**). SWATH-MS quantified proteins with good
248 reproducibility as protein intensities were highly correlated across replicates and adjacent
249 fractions with an average Pearson's R > 0.98 between replicate fractions of the same
250 biological condition (**Supplemental Figure S2B**). The reproducibility of protein abundance
251 measurements was longitudinally affected by deteriorating mass spectrometer performance.
252 However, these progressive effects were efficiently compensated by normalization based on
253 reference spike-in peptides (**Supplemental Figure S2A** and see experimental procedures).
254 The high degree of reproducibility achieved for the overall workflow was further apparent
255 from protein-level SEC chromatograms reconstructed from the independent experimental
256 repeats (See replicate SEC chromatograms of a select set of proteins given in **Figure 3G** and
257 all protein-level chromatograms with error bars provided in **Supplemental Item 1** with
258 source data in **Supplemental Table 1**). Overall, these metrics demonstrate the level of
259 reproducibility of the SEC-SWATH-MS workflow towards the detection of differential
260 protein associations between the two cell cycle states.

261 *Recall of known biology of cell cycle states*

262 Mitotic processes have been extensively studied. We therefore related the results of this study
263 to known mechanisms of mitotic biology, first at the level of general patterns and second at
264 the level of specific complexes. First, we calculated the over representation in gene ontology
265 annotations of the 1793 proteins with shifts detected by SEC. In agreement with previous

266 knowledge the results indicate cell cycle state-dependent changes in the functional groups
267 "RNA splicing and mRNA binding events" (Dominguez et al., 2016), "cellular
268 reorganization" (Gong et al., 2007) and "ribonucleoprotein and macromolecular complexes"
269 (Linder et al., 2017) (**Figure 3B**). Second, we related the results obtained in this study to
270 specific complexes that are known to be present at different assembly states in the cell cycle
271 states tested (Vermeulen et al., 2003). The best confirmed and generally accepted events of
272 this type include the mitotic activation of CDK1 by binding to its partner cyclin B1 (Gavet
273 and Pines, 2010) and the mitotic disassembly of nuclear pore complexes (NPCs) (Linder et
274 al., 2017). We found both events confirmed by the SEC-SWATH data. **Figure 3C** shows the
275 rewiring of the CDK1 - cyclin B1 (CCNB1) module, supported by high differential
276 association testing scores. Specifically, the size-calibrated subunit elution profiles closely
277 reflected the formation of CDK1-CCNB1 complexes in the cell cycle state and indicated that
278 CDK1 subunits of the CDK1-CCNB1 complex were recruited from the monomer pool,
279 whereas the overall expression level of CDK1 across cell cycle states remained stable (**Figure**
280 **3D**). In contrast, CCNB1 subunits showed increased expression in mitosis (**Figure 3D**,
281 insert), consistent with current models of CDK1 regulation by periodic expression of CCNB1
282 (Vermeulen et al., 2003). Notably, only part of mitotic CDK1 transitioned to the complex-
283 assembled form, with 69% detected in the assembled and 31% of the total MS signal detected
284 in the monomeric range. Further, the dataset confirmed the mitotic disassembly of NPCs
285 (**Figure 3E&F**) with 26 of the 27 observed canonical subunits detected as SEC-shifting (out
286 of 32 bona fide components as defined by (Hoelz et al., 2016)). Nucleoporin SEC profiles
287 suggested protein mass re-distribution from a high molecular weight (MW) population of
288 higher order nucleoporin complexes (fraction 5, void volume peak with apparent MW ≥ 5
289 MDa) to lower MW signals representative of NPC sub-complexes. This is exemplified by the
290 SEC elution profiles of the inner ring complex members NUP188, NUP205 and NUP93 that
291 are known to be part of mitotic sub-complexes of the NPC (Linder et al., 2017) (**Figure 3E**).
292 Sub-complexes eluted in earlier fractions of elevated molecular weight compared to the
293 respective monomers (**Figure 3F,** note monomer expected fraction markers). The observed
294 profiles were highly reproducible across the experimental repeats (**Figure 3G**).

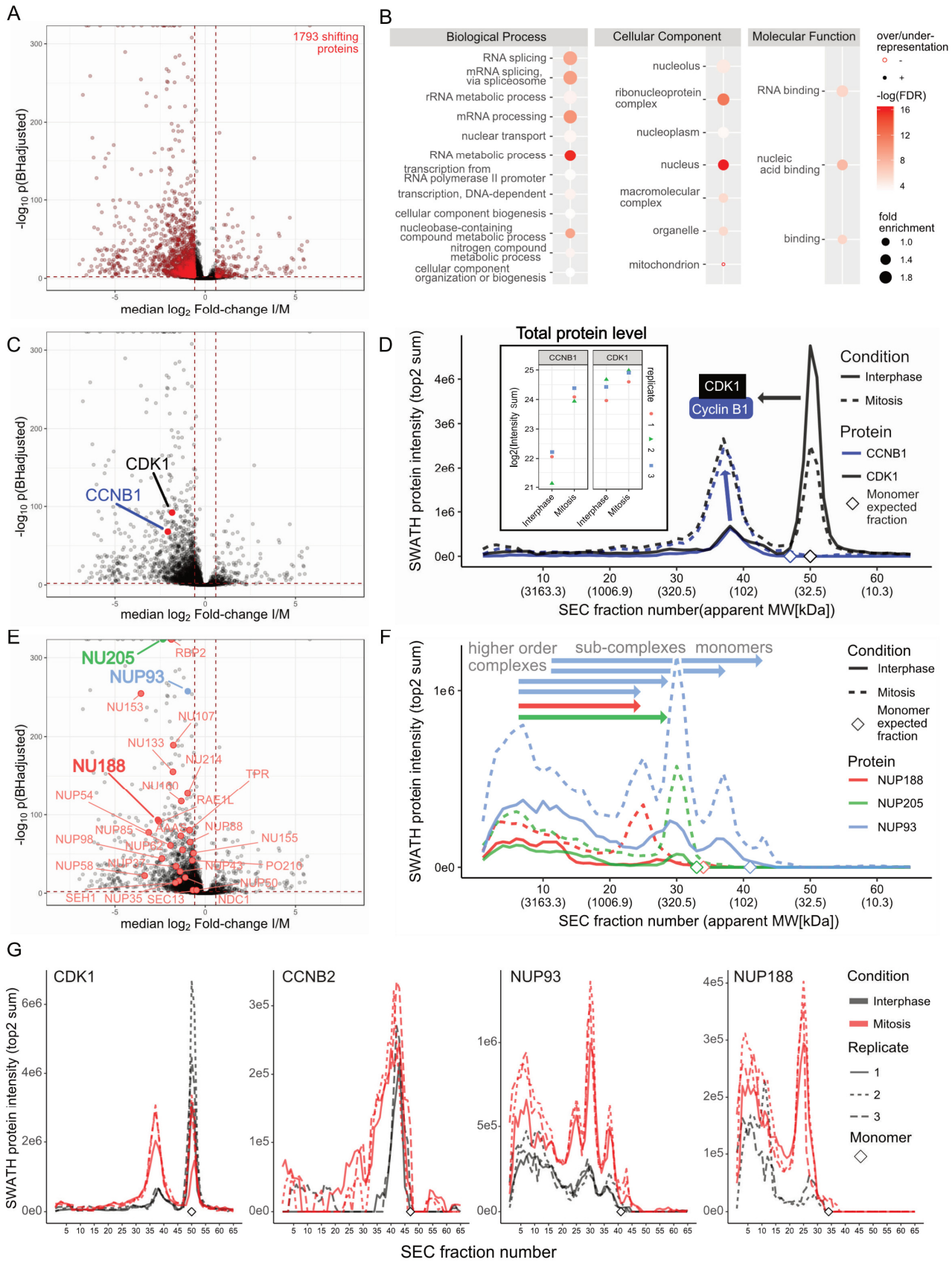

Figure 3: Benchmarking part 1: Recall of expected mitotic complex remodeling events. **A** Protein-level differential association score map highlighting 1,784 proteins shifting quantitative distribution across apparent sized assessed via SEC-SWATH. Benjamini-Hochberg adjusted P-value cutoff, ≤

299 0.01; absolute SEC-localized fold-change ≥ 1.5 -fold. Reproducibility of SEC peptide and protein
300 identification and quantification is assessed in **Figure 1B-D**, protein level error chromatograms
301 (**Supplemental item 1**) and protein intensity correlation (**Supplemental Figure 2A**). **B** Gene ontology
302 analysis of the total set of shifting proteins (PANTHERdb, against the background of all 5,044
303 proteins detected) suggests activity in processes related to cell cycle progression. **C** Protein-level
304 differential association scores for a 'true positive' detection of an instance of mitotic complex
305 remodeling among cell cycle regulators cyclin-dependent kinase 1 (CDK1) and cyclin B1 (CCNB1). **D**
306 Conditional protein-level SEC chromatograms for CDK1 and CCNB1 capture and quantitatively
307 characterize mitosis-specific recruitment of 69% of the CDK1-derived MS-signal (right panel) to the
308 CCNB1-assembled state. Inset: As expected, stable levels of CDK1 are observed while CCNB1
309 appears induced in mitosis (Total intensity observed across the 65 SEC fractions). Diamonds mark the
310 SEC fraction expected for respective monomers based on naked sequence average molecular weight
311 and external size calibration based on reference protein fractionation (compare **Figure 1C**). **E** Protein-
312 level differential association scores for a second instance of 'true positive' detection of mitotic complex
313 remodeling, nuclear pore complex disassembly. 26 of the 27 detectable subunits (out of 32 total, for
314 assignment see experimental procedures) are detected to significantly shift their SEC elution patterns
315 (as assigned in panel **A** and see main text and methods). **F** Conditional protein-level SEC
316 chromatograms for an exemplary subset of protein components of the nuclear pore complex
317 disassembling upon mitotic entry. Protein-centric differential association scores are highlighted in
318 panel **E**. Chromatographic profiles of NUP188, NUP205 and NUP93 reveal protein mass re-
319 distribution from high molecular weight NPC complexes (fraction 5, apparent MW ≥ 5 MDa) to lower
320 MW signals representative of smaller NPC sub-complexes or likely a monomeric pool in the case of
321 NUP93. Diamonds mark fractions where monomer elution would be anticipated.

322 *Validation via orthogonal method.*

323 A significant strength of the present method is its ability to quantify changes in protein
324 complex abundance and chromatographic retention in a highly multiplexed manner. Recently,
325 orthogonal methods have been described that assess thermal stability variation. In this method
326 changes in protein thermostability are used as a proxy for changes in protein interaction and
327 activity. This notion is supported by the observation of strikingly similar thermostability
328 profiles among subunits of the same complex (Tan et al., 2018). Two such studies explored
329 altered thermostability across the cell cycle (Becher et al., 2018; Dai et al., 2018). They used
330 chemical synchronization in early S and prometaphase, thus matching the biological
331 conditions analyzed in the present study. We therefore compared the results obtained by the
332 two orthogonal methods, SEC-SWATH-MS and thermal profiling, represented by two
333 instances of the approach termed Cellular Thermal Shift Assay (CETSA) (Dai et al 2018) and
334 Thermal Protein Profiling (TPP) (Becher et al, 2018).

335 First, we compared the proteome coverage achieved by the respective methods. The SEC-
336 SWATH-MS dataset identified 5044 proteins. Of these 4515 showed detectable SEC elution
337 peak of which after statistical filtering 4480 protein elution profiles were scored (for details
338 on dropouts see experimental procedures). This number is comparable to that achieved by
339 TPP (n = 4779). CETSA achieved a markedly lower coverage at n = 2777 proteins. More than
340 600 proteins were exclusively characterized by SEC-SWATH-MS (**Figure 4A**).

341 Second, for each method we selected the 1000 proteins that showed highest scores indicating
342 mitotic change and compared the observability of expected patterns of mitotic change within
343 this set. For SEC-SWATH-MS the scoring was based on pBHadj/FC rank sum; for CETSA
344 on deltaFC and for TPP on deltaTm (**Figure 4B** and methods section). Whereas the three sets
345 of top ranked proteins method showed a small overlap of 92 of 2409 proteins, the functional
346 and pathway annotation enrichment patterns of the three protein sets were in good agreement
347 between CETSA and SEC-SWATH-MS. Both workflows uncovered changes in "RNA
348 processing", "nuclear transport" and "chromatin organization" processes. The CETSA protein
349 set was also enriched for enzymes involved in "protein methylation and metabolic processes"
350 (**Figure 4D**).

351 Unexpectedly, our analyses suggested lower similarity between the results of the two
352 thermostability based studies compared to the level of agreement between the results from
353 SEC-SWATH-MS and CETSA (206 proteins, 11.5%, shared between CETSA and TPP vs.
354 262 proteins, 15.1%, shared between SEC-SWATH-MS and CETSA, **Figure 4C)**. Cellular
355 component enrichment analysis of the CETSA and TPP results showed increased recovery of
356 membrane-associated proteins by CETSA but not TPP, and strong signals of proteins
357 involved in "macromolecular and ribonucleoprotein complexes" in either dataset (**Figure 4D**,
358 Cellular Component). SEC-SWATH-MS and CETSA showed a strong tendency to uncover
359 proteins known to engage in binding activities, while TPP captured a higher number of
360 transferases, ligases, kinases and other proteins with catalytic activity than CETSA (**Figure**
361 **4D**, Molecular Function). Pathway enrichment analysis showed a similar trend of agreement
362 between SEC-SWATH-MS and CETSA and stronger divergence between CETSA and TPP
363 results. Specifically, both SEC-SWATH-MS and CETSA showed significant enrichment of
364 pathway terms "Cell Cycle / Mitotic Cell Cycle / M Phase" and "nuclear pore complex
365 disassembly" and "nuclear envelope breakdown" among the top scored proteins and only
366 SEC-SWATH-MS captured altered functional states of the core cell-cycle regulator anaphase
367 promoting complex APC/C and activation of the mitotic spindle assembly checkpoint SAC
368 (**Supplemental Figure S3A**).

369 Third, we evaluated the recovery of proteins with known function in the cell-cycle process in
370 the respective datasets (UniProt functional annotation parsed on 'cell cycle', **Figure 4E**). The
371 SEC-SWATH-MS data showed the highest sensitivity for the measurement of altered protein
372 (association) states among the compared methods. (**Figure 4E**, comparing sets from Venn
373 diagram in **Figure 4C**).

374 Fourth, we compared the sensitivity of the methods to recapitulate known biochemical events
375 of mitotic disassembly of NPCs. In this comparison, SEC-SWATH-MS showed the highest
376 degree of sensitivity as nucleoporins were ranked highest in the priority lists compared to the
377 priority lists generated by the other methods (**Figure 4F)**. This comparison validates the SEC-
378 SWATH-MS differential workflow to generate biological insights similar to those obtainable
379 via CETSA and at extended proteome coverage comparable to that achieved in the TPP
380 workflow.

381 Overall, these three levels of benchmarking showed high performance of the SEC-SWATH-
382 MS differential workflow, including the extended CCprofiler tool, to reveal altered protein
383 association states in biological samples with high sensitivity and broad proteomic coverage. In
384 addition, the chromatographic profiles contain extended layers of information such as the
385 specific composition and abundance of distinct complexes and also indicate quantitative
386 changes in protein abundance.

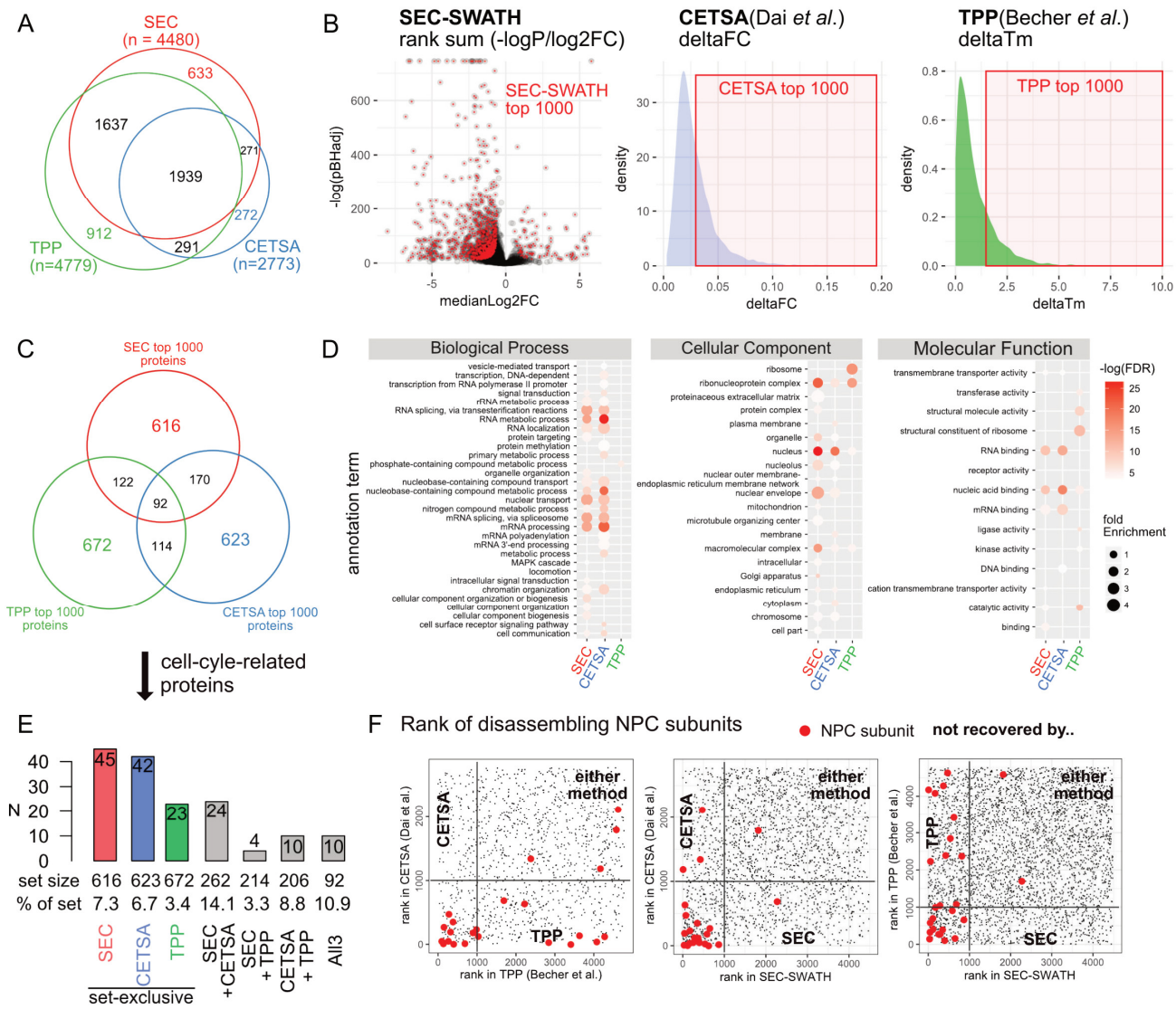

Figure 4: Benchmarking part 2: Performance of measuring proteome state dynamics by apparent size vs. thermostability. **A** Comparison of the total set of proteins characterized in SEC-SWATH (n = 4480, this study), CETSA(Dai et al., 2018) (n = 2773) and TPP(Becher et al., 2018) (n = 4779). **B** Classification of top 1000 proteins to compare method performance. Proteins were ranked according to method-specific scores that intend to capture alterations in proteome association or thermostability state changes between cell populations chemically synchronized in distinct cell cycle stages (Comparison: interphase and prometaphase). All protocols employ thymidine block and nocodazole release experimental regimes. In SEC-SWATH-MS, top 1000 proteins are classified by linear combination of score ranks of equally weighted $\log_{10}$(pBHadj) and median $\log_2$ fold-change and selection along rank sum. Protein thermostability workflows employ two different scores (CETSA: delta fold-change; TPP: delta T_m). The scores of the top1000 proteins selected per method are indicated. **C** Comparison of top1000 association- or stability-changing proteins detected in either approach shows degree of orthogonality and unexpectedly high dissimilarity of the protein sets reported to alter thermostability. **D** Gene ontology annotation enrichment testing of top hit proteins reveals large agreement of detected cellular activity between CETSA and SEC-SWATH, dissimilar

403 results from TPP and a tendency of enzymatic and membrane-associated activity to show rather in
404 altered thermostability than association state assessed via size. TPP preferentially points towards
405 altered states in transferases, ligases and kinases but does not yield significant enrichment of
406 Reactome pathways Cell Cycle / Mitotic Cell Cycle / M Phase in contrast to SEC-SWATH and
407 CETSA (Pathway enrichment is given in **Supplemental Figure 3**). **E** Comparison of ranks of
408 rearranging NPC component proteins in the three methods. Lowest rank means strongest signal in the
409 respective method. SEC-SWATH-MS ranks truly re-arranging proteins preferably. **F** Comparison of
410 method sensitivity based on method-exclusive recovery of 'true positive' proteins which function in
411 relation to the cell cycle. Protein sets from Venn diagram in **C**. Cell-cycle-related proteins were
412 defined by Uniprot annotation column 'Function' parsed on 'cell cycle'. Of these 290 proteins, 158
413 were covered by any or a combination of the compared techniques. Recovered numbers and rates with
414 respect to set size suggest highest sensitivity of SEC and CETSA at overall larger coverage of SEC
415 (4480 proteins scored vs 2773 proteins with scores in CETSA).

416 Inference of cell-cycle dependent complex remodeling

417 We used the quantitative, complex-centric SEC-SWATH technique to detect changes in
418 complex quantity and composition between cell cycle states. These analyses are based on the
419 SEC profiles of 4,515 proteins forming 6,040 distinct peaks (*CCprofiler* protein-centric q-
420 value = 5%, see methods for details) and constitute a global 'master map' set of observable
421 protein features across replicates and conditions (See **Figure 2**B and **Supplemental Figure**
422 **S4A-B**). The chromatographic elution profile of each protein in the master map was analyzed
423 with respect to the following dimensions of information. First, the number of peaks in the
424 chromatographic range covering complex associated proteins indicated a minimal number of
425 distinct complexes a protein was associated with. Second, changes in chromatographic elution
426 between conditions identified proteins with significant changes of complex association, and
427 third, the correlation of peaks in the elution patterns of different proteins confirmed the
428 presence of specific complexes by complex-centric analysis. The data indicated that proteins
429 observed in two or more distinct complex-assembled states were enriched in signaling factors
430 (**Supplemental Figure S3B**), proteins with known binding functions and proteins involved in
431 modulating post-translational modification such as acetylation and phosphorylation
432 (**Supplemental Figure S4D**). The data further indicated that in most cases in which a protein
433 was associated with different complexes the SWATH-MS signals for independent peptides
434 strongly correlated between peaks, indicating overall very robust signal quality. Outlier
435 peptides, i.e. peptides for which the between-peak correlation deviated from the correlation of
436 other peptides, likely indicate cases of post-translational modifications resulting in the
437 differential association of proteoforms to different complexes.

438 The ensemble of protein SEC elution profiles further provided a base to estimate the fraction
439 of the proteome detected in monomeric or assembled form in either state. We designated

440 proteins as detected in an assembled state if their apparent MW based on the SEC elution was
441 minimally twofold larger than the predicted MW of the protein in monomeric form. The
442 protein SEC elution profiles were interrogated from two perspectives. First, we performed a
443 naïve assignment of protein intensity to either complex-assembled or monomeric state. To
444 make these assignments, we used the MS signals of the two most-abundant proteotypic
445 peptides per protein. In line with previous observations of the HEK293 proteome assembly
446 state via SEC-SWATH-MS (Heusel, Bludau et al., 2019), the major fraction of the interphasic
447 and mitotic HeLa CCL2 proteome mass was observed in complex-assembled state (57 ± 6%
448 and 58 ± 4%, respectively). In terms of protein numbers 70 ± 2% and 72 ± 2% of detected
449 proteins were detected at least in part in complex assembled state in interphase and mitosis,
450 respectively.

451 To next explore differences in protein profiles observed between conditions, we applied
452 protein-centric peak detection per each cell cycle state. To increase signal-to-noise we merged
453 the three replicates and detected 5,291 and 5,637 distinct elution peaks for 4,083 and 4,264
454 proteins in interphase and mitosis, respectively. Based on the apex SEC fraction and
455 associated apparent molecular weight, the 1-5 elution peaks observed per protein were
456 assigned to likely assembled or monomeric pools of the total protein population (**Figure 5A**).
457 According to these assignments, 29 and 25% of proteins were observed eluting exclusively in
458 monomeric form, while 71 and 75% of proteins were observed in at least one complex-
459 assembled form in interphase and mitosis, respectively. A significant fraction of proteins was
460 further observed eluting in both, monomeric and complex assembled form(s) (12% in both
461 interphase and mitosis, respectively). These results indicate that in either cell cycle state a
462 significant fraction of the proteome was associated with complexes that are accessible to
463 differential quantification of protein association state changes via SEC-SWATH-MS and
464 *CCprofiler*.

465 We further used the ensemble of protein patterns to determine which proteins and associated
466 functions displayed a change in protein complex association between the two cell cycle states
467 tested. The data indicated substantial rearrangement of the proteome. Specifically, 2,189 SEC
468 elution peaks of 1,793 proteins showed significant abundance shifts. Of these, 1,626 shifts
469 were in the SEC elution range of complex-assembled proteins suggesting significant
470 rearrangements in the underlying complex(es) (**Figure 3A**, pBHadj score ≤ 0.01, absolute
471 SEC-localized fold-change ≥ 1.5). Proteins with altered complex association states were
472 predominantly associated with functions in "transcriptional and splice regulatory machinery"
473 and "cellular component organization" (**Figure 3B)**. The 1000 top-ranking proteins selected
474 for comparative benchmarking analyses further revealed reorganization in the MAPK cascade
475 (**Figure 4D**, Biological Process) and rearrangements involving central cell-cycle-associated

476 modules such as the APC/C, NPC and mitotic spindle checkpoint and mitotic anaphase
477 pathways, among others (**Figure S3A**).

478 Whereas these enrichment analyses already pointed at specific complexes undergoing mitotic
479 change, we next evaluated our results using the CORUM reference set of complexes as prior
480 information (Ruepp et al., 2010). Initially, we evaluated the rearrangements detected by SEC-
481 SWATH-MS that occur preferentially among protein complexes with known involvement in
482 mitotic processes. Indeed, we detected a higher frequency of changed patterns of proteins that
483 are known to associate into complexes, compared to a control group not known to be
484 affiliated with a complex (**Figure 5B**). On the level of individual proteins, the SEC-SWATH-
485 MS dataset covered over half of the subunits of the reference CORUM complexes (1473 of
486 2937). Of these, 702 showed significant changes in protein complex association between
487 states (**Figure 5C**, upper panel). More than half of the reference complexes were detected
488 based on two or more subunit proteins in our analysis (n = 949, **Figure 5C**, lower panel and
489 **Figure 5D**). Overall, 432 complexes showed evidence of remodeling based on significant
490 SEC shifts observed for minimally two of their subunits (**Figure 5E**). Among these changing
491 complexes, we observed preferential and more complete detection of changes in complexes
492 with known involvement in the cell cycle (**Figure 5F**). While many of the complexes with
493 evidence of remodeling are associated with known functions in relation to the cell cycle, a
494 significant fraction is not and thus present opportunities for further exploration. The
495 remodeled complexes and their functional annotation are summarized in **Supplemental Table**
496 **2**.

497 The results in **Figure 5G&H** illustrate two complexes without GO annotation for "cell cycle"
498 but with strong evidence for mitotic changes. For both complexes all CORUM subunits were
499 detected. The first is the cell-cycle-dependent assembly of the TRF2-RAP1 complex in
500 mitosis observed by strong SEC shift scores of both subunits and co-elution of RAP1 and
501 TRF2 with apex in SEC fraction 21 (ca. 950 kDa) in mitotic cells but not interphasic cells.
502 TRF2 was detected only in mitotic cells. In interphasic cells, RAP1 and showed no peak in
503 the SEC fraction range of the TRF2-RAP1 complex (**Figure 5G**). The results are in line with
504 the previously reported recruitment of RAP1 to telomeres via TRF2 and consistent with the
505 co-elution of the two proteins in the void volume (fractions 1-5, analytes >10 MDa) (**Figure**
506 **5G**, right panels). However, RAP1 was detected in the void volume of interphasic cells but
507 without the concurrent detection of TRF2. Notably, we did not observe the TRF2 and RAP1-
508 containing shelterin complex known to occupy telomeres in interphase (Liu et al., 2004),
509 likely due to low abundance and/or low recovery in mild lysis of interphase cells. In either
510 cell cycle state, RAP1 was observed with an apparent molecular weight of ~180 kDa, in line
511 with preassembly into the tetrameric form in which it participates to form the octameric

512 TRF2-RAP1 complex composed of four copies of each protein (Arat and Griffith, 2012). In
513 mitotic cells, the strongest peak group containing RAP1 and TRF2 centered around 950 kDa,
514 ca. 2.5x the weight expected for TRF2-RAP1 hetero-octamers, suggesting the association of
515 the octamer with as yet unknown proteins. Notably, RAP1 has been known to associate with
516 the I-kappa-B-kinase (IKK) complex to enhance NF-kappa-B target gene expression (Teo et
517 al., 2010). To test whether the observed 950 kDa signal reflected the RAP1 pool likely
518 engaged in an interaction with the IKK complex, we considered in addition the elution
519 profiles of IKK subunits CHUK and IKKB (**Figure S5A**). The CHUK and IKKB profiles
520 suggest the presence of two distinctly sized and only partly SEC-resolved variants of the IKK
521 complex, one of ca. 2.5 MDa (apex fraction 12) and one of ca. 1.7 MDa (apex fraction 16)
522 (**Figure S5A**). The majority of the RAP1 signal at ca. 950 kDa appeared independent from the
523 two distinct populations of IKK complex variants observed. However, a peak shoulder in the
524 RAP1 signal at elevated molecular weight (estimated apex fraction 16) conformed with a
525 small fraction of RAP1 bound to the 1.7 MDa but not the 2.5 MDa variant of the IKK
526 complex (**Figure S5A,** lower panel, fractions 14-18).

527 As a second example, we observed striking changes in the elution profile of the Nup107-160
528 sub-complex of the NPC (Corum ID 87, **Figure 5H**). All 9 subunits were detected with
529 significant SEC shifts (**Figure 5H**, middle panel). In mitotic cells, the complex was observed
530 based on a co-elution peak group formed by all subunits at a molecular weight of 2.8 MDa
531 (Apex fraction 13, **Figure 5H**, right panel). In interphase cells, no defined co-elution peak
532 was detected in this size range, suggesting the presence of the Nup107-160 sub-complex
533 exclusively in mitotic extracts. Interestingly, the subunit SEC13 was observed in a second
534 peak at ~ 1 MDa in both cell cycle states, suggesting its presence in an additional complex
535 resolved by SEC. We surmised that this peak may represent SEC13 in the context of its
536 alternative functional role in COPII vesicle-mediated transport (Tang et al., 1997). To test this
537 hypothesis, we overlayed the elution profiles of the SEC13 partners in the coatomer complex
538 and, indeed, observe co-elution with its partner SEC31 but not with the adaptor proteins
539 SEC23A/B and SEC24/B (See **Supplemental Figure S6**). These observations demonstrate
540 the capacity of our method to capture mitotic liberation of Nup107-160 sub-complexes from
541 NPCs in and to resolve protein engagement across different functional contexts. Mitotic
542 disassembly of NPCs is a hallmark of mitotic progression (Linder et al., 2017) but this event
543 has not been annotated in the respective GO terms. This insight into complex dynamics at
544 sub-complex resolution led us to explore whether SEC-SWATH-MS chromatographic
545 profiling could reveal further and potentially novel aspects of mitotic NPC disassembly (see
546 below).

547 In summary, these results show that a major portion of the proteome changes at the level of
548 complex association between mitotic states and that hundreds of specific complex remodeling
549 events were apparent from the data. Insights at sub-complex resolution warrant in-depth
550 analysis of chromatographic profiles not only for newly implicated proteins but may also
551 reveal novel or additional roles of proteins with known functions in cell cycle progression.

552

553 *Figure 5: Inference of cell-cycle dependent complex remodeling.* **A** Global proteome assembly states

554 observed in interphase and mitosis. Barplots show numbers of proteins eluting in one to five distinct

555 peaks. Pie charts show that the majority of proteins peak at least once in the likely complex-assembled
556 range (apparent molecular weight twice or larger than the annotated monomer molecular weight). In
557 either cell cycle state, 12% of the proteins are observed in both monomeric and complex-assembled
558 state and ca. 30 % of the proteins elute in two or more distinct peaks, in line with previous
559 observations on the HEK293 proteome modularity profiled by SEC-SWATH-MS (Heusel, Bludau et
560 al., 2019). Peak detection was strictly error-controlled (q-value FDR estimate of 5 %) against
561 randomized peptide-to-protein associations. For details, see experimental procedures. **B** Preferential
562 detection of shifts in proteins that are subunits of known reference complexes of the CORUM database
563 displayed based on the proteins SEC shift score ranks. Proteins that under certain conditions integrate
564 into complexes display lower ranks, with rank 1 representing the highest SEC shift score observed. **C**
565 Coverage of CORUM reference complexes in SEC-SWATH-MS. Upper chart: Coverage on the level
566 of complex component subunits. Lower chart: Coverage on the level of complexes (covered if two or
567 more of the annotated subunits were among the SEC-SWATH-MS results). **D** The 949 complexes
568 covered in the dataset with two or more subunits. For visualization purposes, the complexes are
569 represented by the complex-level means of subunit-level differential SEC shift scores. **E** The 432
570 complexes that were detected to undergo remodeling in mitosis vs. interphase, based on significant
571 SEC shifts of minimally two of their component subunit proteins. For visualization purposes, the
572 complexes are represented by the complex-level means of subunit-level differential SEC shift scores.
573 The coloring indicated whether the complex is annotated with "cell cycle" in the database-contained
574 gene ontology terms (GO). **F** For the changing complexes, the fraction of shifting subunits (of those
575 detected by SEC-SWATH-MS) was plotted as function of complex size (n subunits, detected by SEC-
576 SWATH-MS) and whether or not the complex bears the GO annotation 'cell cycle'. Shift completeness
577 is higher among cell cycle-related assemblies. **G** Example of a complex that is remodeling along the
578 cell cycle states but not annotated with 'cell cycle', TRF2-Rap1 complex III (CORUM ID 1205),
579 showing a representative spokes model, subunit protein level SEC-shift scores in the context of all
580 observed shift scores and their quantitative elution along SEC as profiled by SWATH-MS. Both
581 subunits display significant SEC shifts. The analysis detects a co-elution signal indicating the presence
582 of a complex of ca. 950 kDa (Apex fraction 21) in mitosis but not in interphase, where only RAP1 is
583 detected. **H** Equivalent to panel G. Second example of a complex that is remodeling along the cell
584 cycle states but not annotated with 'cell cycle', Nup107-160 subcomplex (CORUM ID 87), showing a
585 representative spokes model, subunit protein level SEC-shift scores in the context of all observed shift
586 scores and their quantitative elution along SEC as profiled by SWATH-MS. All 9 subunits display
587 significant SEC shifts. The Nup107-160 sub-complex appears specifically in mitosis and with an
588 apparent molecular weight of 2.8 MDa (Apex fraction 13, right panel). Subunit SEC13 shows an
589 additional peak at ca. 10 MDa (Apex fraction 20-21) where it appears bound to its partner subunit in
590 its alternative context in the COPII complex, SEC31 (**Supplemental Figure S6**).

591 ## Discovery and independent validation of NPC disassembly intermediates

592 The discovery of compositional rearrangements of protein complexes between cell cycle
593 states allowed us to propose testable changes of biochemical processes. Among these is the
594 mitotic disassembly of the NPC (Hoelz et al., 2016). The ensemble of SEC protein profiles
595 analyzed in this study contained 27 of the 32 bona fide NPC components (Hoelz et al., 2016),
596 shown in **Figure 6A** in either state. The patterns show a general, distinctive change towards
597 complexes of lower MW in the mitotic sample, consistent with NPC disassembly into sub-
598 complexes. All but one of the detected subunits (NUP50) showed shifts in protein-centric
599 differential scoring. For eight of the subunits, elution peaks in the monomeric range were
600 detected, equally across both cell cycle states. The observation of monomeric pools in the
601 SEC experiment may indicate the presence of a subset of NPC components that seem to be
602 present in the cell as assembly-competent monomeric forms, to potentially bind other partners
603 to fulfill other functions or liberated from partner Nups during preparation of the cell extracts.

604 Due to the distinctive pattern changes between the two states tested, we focused on the key
605 inner ring complex component NUP93, which functions as an adaptor between the NPC
606 scaffold and the central channel FG Nup62-Nup58-Nup54 sub-complex. In interphase
607 extracts, NUP93 was principally detected in a wide high MW peak (fractions 1-15, > 10 MDa
608 to ca. 1.8 MDa) apart from minor amounts detected in two lower MW populations (apex
609 fraction 29, ~ 360 kDa and apex fraction 37, ~145 kDa). In the mitotic state, NUP93 was
610 detected in three distinct lower MW SEC peaks, with a new signal at an apparent MW of ca.
611 570 kDa (elution range F21-F27) and two signals of increased intensity when compared to the
612 interphase pattern at apparent MW of ca. 320 kDa (elution range F27-F33) and 145 kDa
613 (elution range F35-F39) (**Figure 3F**, **Supplemental Figure S5B** and schematically illustrated
614 in **Figure 6B**). The observed peak pattern indicates that in mitotic cells NUP93 associates
615 with complexes of different size that elute markedly earlier than monomeric NUP93 (93.5
616 kDa, expected elution fraction 41), thus suggesting the formation of distinctive NUP
617 disassembly intermediates containing NUP93. To infer the composition of these complexes,
618 we locally correlated the elution pattern of NUP93 with the elution patterns of other Nups
619 (**Figure 6B**). For the peak at ca. 320 kDa, this analysis suggested NUP205, NUP155 and
620 NUP214 as NUP93 interaction partners (F27-33, **Figure 6B**, right panels). Similarly, for the
621 peak at ca. 570 kDa, (**Figure 6B** left panel), six proteins, namely the central channel FG Nups
622 NUP62, NUP54 and NUP58 as well as NUP188, NUP50 and TPR eluted in the same peak as
623 NUP93.

624 The relative mass spectrometric signal intensities of peptides can be used to estimate the
625 abundance of a protein in a SEC peak (Ludwig and Aebersold; Rosenberger et al., 2014**).** For
626 the peak at ca. 320 kDa quantification of the respective protein signal intensities identified the

627 inner ring proteins NUP155 and NUP205 as the predominant binding partners of NUP93. In
628 contrast, NUP214, whose quantitative pattern correlates well in the SEC dimension, is present
629 at much lower signal intensity which is not consistent with stoichiometric participation in the
630 complex. The results thus suggest a complex dissociating from the NPC holo-complex in
631 mitosis that is composed of NUP93, NUP155 and NUP205. Notably, NUP188 displays only
632 low local correlation with NUP93 in the queried target range, suggesting that NUP188 does
633 not participate in the complex of ~320 kDa detected between F27 and F33 (**Figure 6B**, right
634 panel). The observed MW of 320 kDa is smaller than the cumulative weight of a
635 stoichiometric hetero-trimer (476 kDa). This discrepancy could be due to compact shape
636 and/or interactions with the stationary phase. Similarly, we used the protein intensities to also
637 estimate composition and the abundances of the proteins in the peak at ca. 570 kDa (**Figure**
638 **6B** left panel). The data suggest that in this complex the inner ring component NUP93 was
639 associated with the central channel sub-complex NUP62, NUP54 and NUP58, as well its
640 inner ring complex partner subunit NUP188. Based on the absolute signal intensity,
641 stoichiometric participation of TPR in the ~570 kDa assembly appears unlikely. These
642 findings are supported by current models of NPC structure (Beck and Hurt, 2017; Hoelz et al.,
643 2016; Lin et al., 2016) in which central channel Nups are coordinated by adaptor Nups of the
644 inner ring complex. Based on the holo-complex model, the recovery of both TPR and NUP50
645 as part of NUP93-containing complexes appears unlikely, whereas interaction between
646 NUP93 and central channel appears probable because NUP93 serves as anchor point for the
647 central channel within the NPC holo-complex (Chug et al., 2015; Hoelz et al., 2016; Lin et al.,
648 2016).

649 We validated the existence of the previously unknown mitotic sub-complex consisting of
650 NUP93, NUP188 and the trimeric central channel sub-complex NUP62-NUP58-NUP54 by
651 co-precipitation coupled to immunoblotting or mass spectrometry as orthogonal methods. We
652 inducibly expressed HA-St-tagged NUP58 in HeLa cells synchronized in either interphase or
653 mitosis. As a control for the completeness of mitotic arrest, we performed immunoblots of
654 NUP53 in the input samples, demonstrating its efficient mitotic hyper-phosphorylation, as
655 previously reported (Linder et al., 2017). We isolated the native complex associated with the
656 tagged Nup58 under mild conditions and tested the isolate for the presence of the suggested
657 complex components by immunoblotting and LC-MS/MS in either cell cycle state (**Figure**
658 **6C&D** , **Supplemental Figure S1D&E)**. Indeed, immunoblotting confirmed co-purification
659 of both the immediate partner Nups (NUP62, NUP54) and the inner ring complex components
660 NUP93 and NUP188 with NUP58 from interphase cells. Importantly, in mitosis, this
661 connectivity was maintained, in agreement with our SEC-SWATH-MS results (**Figure 3C**).
662 These data confirm the presence of a mitotic sub-complex involving both central channel and

663 inner ring complex components NUP93 and NUP188. The observed relative signal intensities
664 in immunoblotting show a reduced recovery of NUP93 with the central channel Nups in
665 mitosis compared to interphase. This is consistent with mitotic partitioning of the NUP93
666 protein pool across multiple macromolecular entities, as indicated by SEC-SWATH-MS
667 (**Figure 3C**, rightmost two lanes and compare **Figure 6B**, right panel).

668 Next, we analyzed proteins co-isolated with Nup58 by mass spectrometry and used the
669 number of identified mass spectra as semi-quantitative measure to estimate protein retrieval
670 from cells in either cell cycle state and respective controls. The results further confirmed the
671 co-purification of NUP93 and NUP188 and also showed the presence of the inner ring
672 complex component NUP205 (**Figure 6D**). Notably, NUP205 was consistently detected in the
673 SEC elution range under investigation (F21-F27) but did not show a distinctive co-elution
674 peak. Neither NUP50 nor TPR were detected as significant components of the isolates and are
675 unlikely to represent *bona fide* components of the new sub-complex. (**Figure 6D**). Thus,
676 Nup50 is likely part of a different, independent protein complex eluting at a similar position
677 in SEC, which can motivate future research on the mitotic fate of this Nup.

678 Together, these results indicate that, in contrast to preceding models of NPC disassembly, a
679 fraction of the inner ring complex components NUP93 and NUP188 and likely NUP205
680 remain attached to the central channel sub-complex composed of NUP62, NUP58 and NUP54
681 after mitotic entry. This configuration can explain how central channel Nups are efficiently
682 reincorporated into reforming NPCs along with their partner scaffold Nups during mitotic
683 exit. Further, a second population of NUP93 is stored in a mitotic sub-complex with the
684 canonical IRC components NUP155 and NUP205 in absence of NUP188 (See model in
685 **Figure 6E**).

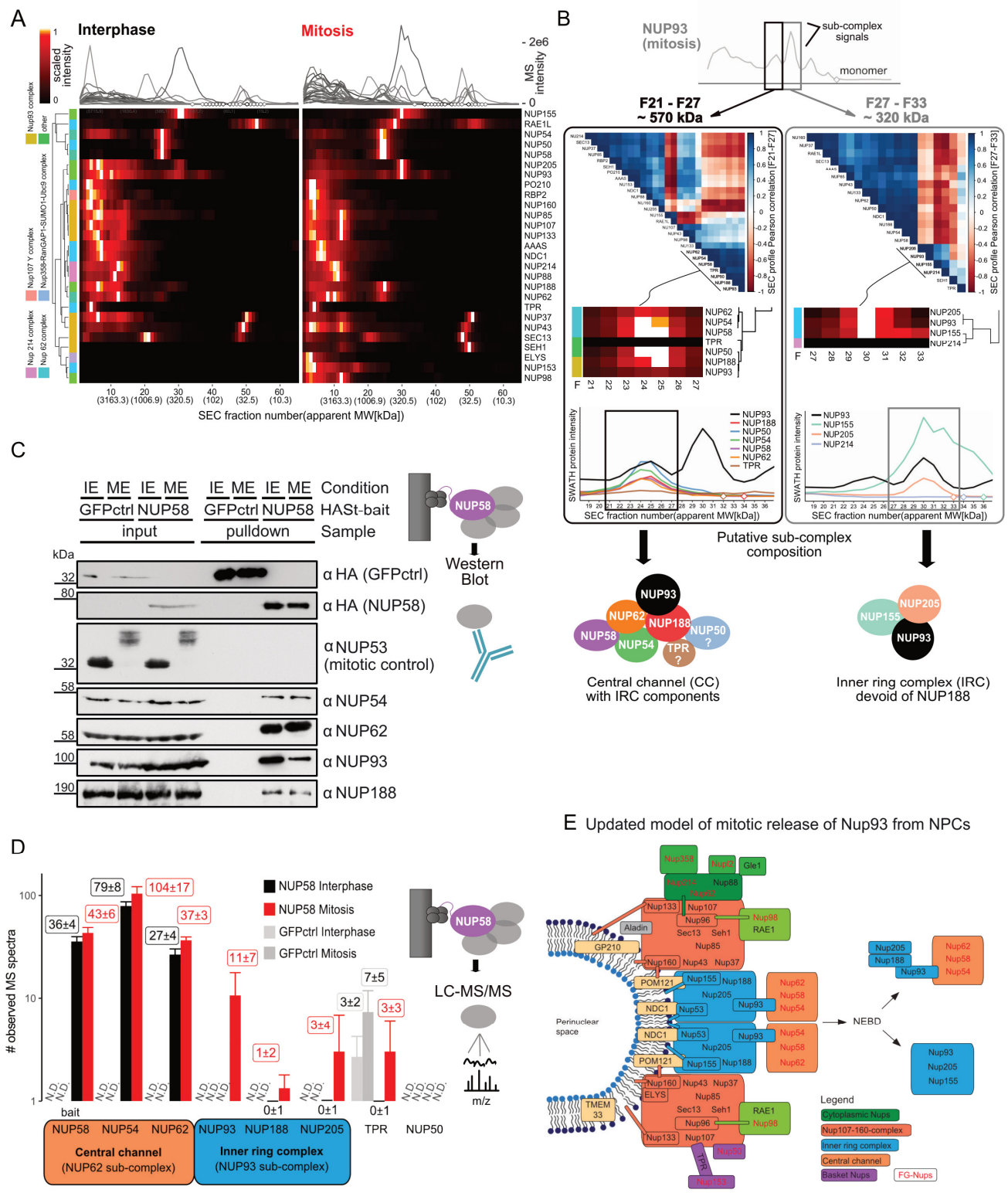

Figure 6: Discovery and independent validation of NPC disassembly intermediate. **A** Quantitative elution patterns of NPC subunits in interphase and mitosis display protein mass re-distribution from large nucleoporin complexes in interphase with void volume elution (> 5MDa) towards lower MW ranges larger than individual components, in line with NPC disassembly into defined sub-complexes. Also compare Figure 3F. **B** Targeted search for co-eluting proteins as candidate co-complex members, using as basis two of the mitotically induced sub-complex signals arising from the inner ring complex

693 component NUP93. Left panel: MS signal correlation analysis in the first peak (apex fraction, 25;
694 apparent MW, ca. 570 kDa; elution range, F21-F27) nominates candidate members of the sub-complex
695 eluting in signal 1 based on co-elution. Right panel, co-elution-based nomination of additional sub-
696 complex membership candidates for signal 2 (apex fraction, 30; apparent MW, 320 kDa; elution range
697 F27-F33). Bottom, putative sub-complex composition subjected to validation experiments (see panels
698 C&D). Note that targeted search for co-eluting proteins (on global dataset scale) is a core function of
699 our online data interrogation tool SECexplorer-cc. **C** Testing mitotic sub-complex composition based
700 on co-purification with central channel complex captured via NUP58 by immunoblotting. As mitotic
701 control NUP53 was included and complete size shifts indicate high homogeneity of cell cycle state of
702 the analyzed cell populations in interphase (IE) and mitosis (ME). As negative control to control for
703 non-specifically bound background protein, green fluorescent protein was included. Both NUP93 and
704 NUP188 co-purify with the central channel in interphase and continue to do so in mitosis, confirming
705 the results from SEC-SWATH-MS. D Testing mitotic sub-complex composition based on co-
706 purification of Nups with the central channel complex captured via NUP58 by mass spectrometry (AP-
707 MS). The number of identified mass spectra serves as semi-quantitative measure to estimate protein
708 retrieval from cells in either cell cycle state and respective controls. The results confirmed the co-
709 purification of NUP93 and NUP188 and also showed the presence of the inner ring complex
710 component NUP205. which is detected in SEC but does not form a defined elution peak in the signal 1
711 range. Neither TPR nor NUP50 are recovered in amounts above background binding level and are thus
712 likely not part of the mitotic NPC sub-complex. E Model of mitotic NPC disassembly and storage of
713 NUP93 in distinct mitotic sub-complex reservoirs before re-formation of daughter cell nuclear
714 envelopes. A substantial fraction of NUP93 is stored in the newly identified mitotic sub-complex
715 composed of central channel components NUP54, NUP58 and NUP62 as well as inner ring complex
716 components NUP93, NUP188 and NUP205.

717 Browsing dynamic complex association maps in SECexplorer-cc

718 SEC-SWATH-MS portrays the process of mitosis from the angle of protein mass re-
719 distribution across differently sized stable complexes resolved by SEC. There remains a lot to
720 be learned from the rich dataset generated, with the prospect of discovering new proteins
721 involved in cell cycle regulation and of identifying new components of both static as well as
722 dynamic assemblies. To support community-based mining and interpretation of our dataset,
723 we provide a web tool, *SECexplorer-cc* (https://sec-explorer.shinyapps.io/hela_cellcycle/,
724 **Figure 7**) which offers four functionalities: (i) Interactive viewing of protein SEC
725 fractionation profiles in interphase and mitosis (compare **Figure 3D** and **F**). (ii) Search for
726 locally co-eluting proteins to identify putative new binding partners showing strong co-elution
727 within a certain range of target protein elution (compare **Figure 6B**). (iii) Interactive display
728 and protein selection from the differential association score map (compare **Figure 3A**). (iv)
729 Display of one or multiple protein's fractionation profiles in reference to the profiles of
730 immediate interaction and/or functional partners dynamically retrieved from StringDB

731 (Szklarczyk et al., 2017). We expect that SECexplorer-cc will support a community effort to
732 fully leverage the rich information encoded by the mitotic proteome rearrangement SEC-
733 SWATH-MS data, which, ideally, will support better understanding of modular proteome
734 function along cell division.

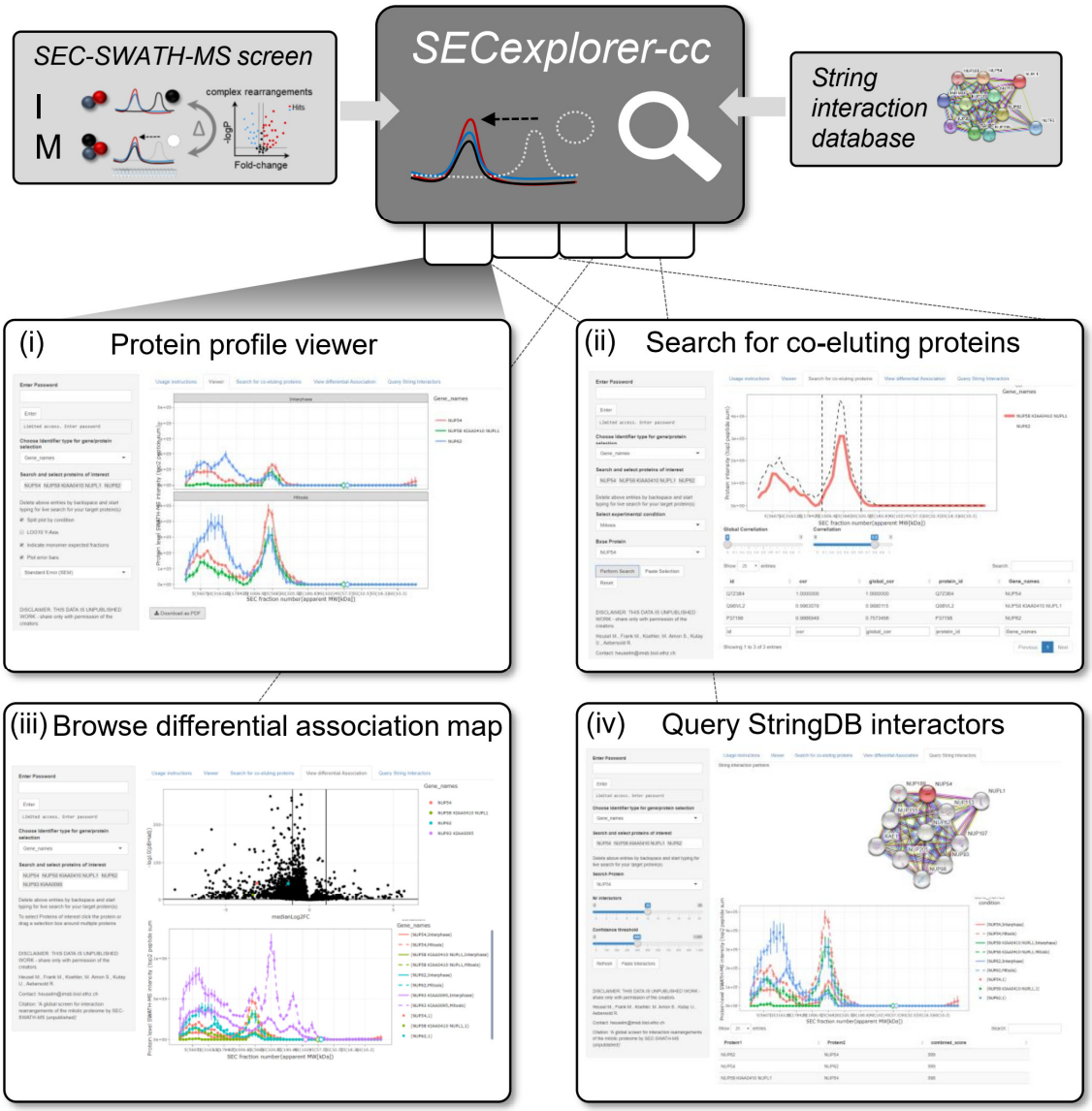

735

736 *Figure 7: Browsing dynamic complex association maps in SECexplorer-cc.* Overview of
737 *SECexplorer-cc*, a web tool that allows to browse and rapidly interrogate differential SEC-
738 SWATH-MS datasets to support researches in customized hypothesis testing. SECexplorer-cc
739 currently combines the dynamic cell-cycle proteome association map reported here and
740 integrates it with information from the String database (Szklarczyk et al., 2017). *SECexplorer-*
741 *cc* features four core functionalities. **(i)** Interactive display and hit protein selection from the
742 statistical SEC shift score map. **(ii)** Semi-targeted search for locally co-eluting proteins to
743 identify putative new binding partners showing strong co-elution within a certain range of
744 target protein elution. **(iii)** Display of custom protein sets conditional fractionation profiles.

745 **(iv)** Display of one or multiple hit protein's fractionation profiles in reference to its immediate
746 functional and/or physical interaction partners obtained StringDB to discover potential
747 physical association among functionally related proteins and to add cellular context
748 information.

749 Discussion

750 The biochemical state of a cell is the result of the ensemble of biochemical functions which in
751 turn are largely carried out by macromolecular complexes. Changes in the quantity,
752 composition, subunit topology or structure of such complexes are thus assumed to reflect
753 altered functional states of the cell and the systematic detection of such alterations is therefore
754 of great interest for basic and translational research.

755 In this study we introduce a new software module to the *CCprofiler* suite (Heusel, Bludau et
756 al, 2019) that supports the differential, quantitative analysis of thousands of proteins and their
757 association with complexes from SEC-SWATH-MS datasets, based on a complex-centric
758 analysis strategy. We benchmarked the tool and applied it to detect rearrangements protein
759 complexes in a differential analysis of human cells in two chemically induced cellular states,
760 interphase and mitosis/early prometaphase. The described technique is based on the co-
761 fractionation and protein correlation profiling rationale (Dong et al., 2008; Foster et al., 2006;
762 Liu et al., 2008; Wessels et al., 2009) and includes the improvements with regard to
763 chromatographic resolution, accurate data-independent mass spectrometry (Gillet et al., 2012;
764 Röst et al., 2014) and complex-centric data analysis strategy implemented in SEC-SWATH-
765 MS (Heusel and Bludau et al., 2019). Through the addition of the quantification module, the
766 workflow now supports the systems-wide differential analysis of > 5,000 of proteins and their
767 association with complexes. The data show that the system shows a high degree of
768 reproducibility and performs favorably when benchmarked against protein thermostability
769 measurements, an orthogonal state-of-the-art method to infer changes in protein complexes
770 (Becher et al., 2018; Dai et al., 2018). Application of the method to HeLa CCL2 cells
771 recapitulated known cell cycle-dependent complex remodeling events between the cell cycle
772 states tested and suggested a new model of nuclear pore complex disassembly which was
773 subsequently validated by orthogonal methods, thus demonstrating the potential of the method
774 and dataset to reveal new biology. To support additional exploration of the present data set
775 and future differential SEC-SWATH datasets, we provide an online tool, SECexplorer-cc.

776 To retrieve information on changes in protein complex quantity and composition, we devised
777 a protein-centric differential analysis strategy that detects altered SEC distribution patterns of
778 ca. 5,000 proteins. Changes in these elution patterns between conditions indicated changes in
779 the association of the respective protein with different complexes and such events could be

780 quantitatively compared between states using the new quantification module implementing a
781 strategy we term differential association testing. This computational pipeline was devised to
782 achieve (i) optimal sensitivity to recall changes based on all available peptide-level
783 information and (ii) maximal coverage by not restricting the differential analysis on
784 previously known protein complexes. With more than 90% of the identified proteins being
785 represented as quantitative SEC elution peaks, the method achieved broad coverage of
786 biological functions. The protein-centric differential analysis pipeline is implemented as
787 additional module of our R/CCprofiler toolset, available at
788 https://github.com/CCprofiler/CCprofiler/tree/helaCC).

789 To benchmark the method we compared the differential SEC-SWATH-MS data obtained in
790 this study with results of two studies that investigated cell-cycle-associated changes in protein
791 complexes through inference from protein thermostability changes measured in similarly
792 perturbed cell systems (TPP and CETSA, (Becher et al., 2018; Dai et al., 2018)). The TPP and
793 SEC studies used HeLa cells (TPP; HeLa Kyoto; SEC, HeLa CCL2) and the CETSA study
794 used K562 cells. Under the assumption of strong conservation of the mitotic regulatory
795 circuitry between the cells tested, our comparison suggests favorable sensitivity to recall
796 known cell cycle dependent complex rearrangement events of the SEC-SWATH-MS method.
797 However, generic conclusions on the relative merits of apparent size vs. thermostability of
798 protein complexes is beset by the observed discrepancy in the results obtained via the two
799 thermostability-centered approaches. Surprisingly, we observe a higher similarity between
800 processes detected by SEC-SWATH-MS and CETSA, than between CETSA and TPP (Dai et
801 al., 2018). Our results give first insights into the biological information gleaned from the two
802 approaches to infer altered protein complexes between states. For example, activity in
803 enzymatic and metabolic processes preferentially showed on the level of altered protein
804 thermostability and was detectable by SEC-SWATH-MS to a lesser extent. Furthermore, the
805 measurement of thermostability via CETSA captured changes in membrane- and DNA-
806 associated proteins that were less efficiently profiled via the SEC-SWATH-MS workflow
807 (**Figure 4D**). In contrast, only SEC-SWATH-MS recovered altered activity patterns of a
808 number of cell cycle pathways not recovered by either of the thermostability-based
809 approaches, such as e.g. increased formation of translation initiation complexes or the
810 inactivation of APC/C complex. Overall the data suggest that SEC, as implemented in the
811 SEC-SWATH-MS workflow, currently offers a preferable combination of analytical breadth
812 and sensitivity.

813 Our study generated new and confirmed known biological insights. For example, only a
814 subset of the CDK1 pool is recruited to upregulated CCNB1 in mitosis (31% appear to remain
815 monomeric, compare **Figure 3D**). This effect cannot be attributed to incomplete

816 synchronization of the analyzed cell populations. We surmise that the degree of assembly acts
817 as an additional layer of CDK1 activity control by defining the cellular concentration of
818 assembled CCNB1-CDK1 complexes that can be transferred to an active state by protein
819 phosphorylation (Nigg, 1993). This notion is relevant for ongoing drug development
820 programs that target the respective interaction interfaces as alternative anticancer strategy
821 (Peyressatre et al., 2015).

822 Differential SEC-SWATH-MS data also illustrated the process of mitotic disassembly of
823 NPCs into distinctive sub-complexes. This allowed us to identify a novel mitotic sub-complex
824 and to extend the model for mitotic NPC disassembly (Laurell et al., 2011; Linder et al.,
825 2017). These observations from the SEC-SWATH dataset were further confirmed with
826 orthogonal methods. Even though several publications reported mechanistic insights into the
827 phosphorylation-driven process of mitotic NPC disassembly (Laurell et al., 2011; Linder et
828 al., 2017), the overall process remains incompletely understood. NPC disassembly must
829 liberate Nups in a state in which they are readily available for rapid reassembly during mitotic
830 exit. Our discovery of a mitotic protein complex between central channel FG-Nups and their
831 anchoring scaffold Nups indicates that the efficient incorporation of the FG Nups may occur
832 together with their anchoring partners. Such mechanism would be ideally suited to explain
833 correct and rapid reassembly during mitotic exit. In this scenario, reintegration will rely on a
834 larger set of protein interactions directed by the scaffold subunits. Detailed knowledge about
835 the mechanistic rules of mitotic NPC disassembly and interphasic re-assembly may well
836 prove helpful in the design of future therapies aiming to modulate the process of cell division.

837 The specific complexes discussed in this paper, including the novel NPC disassembly
838 intermediates only represent a small fraction of the information contained in the dataset of
839 5,044 proteins of which 1,793 showed significantly different association with complexes
840 across the two cell cycle states analyzed. To support further in depth interrogation of the
841 dataset we disseminate it in an easily browsable form via *SECexplorer-cc*. To infer strong
842 hypotheses on novel players that justify at times costly and lengthy follow-up experiments, it
843 is important to bear in mind inherent limitations of and potential confounding effects in the
844 experimental system. These include i) differential extractability of proteins due to cellular re-
845 organization, exemplified by breakdown of the nuclear envelope upon mitotic entry, ii)
846 indirect effects, i.e. rearrangement as a mere consequence rather than cause of the altered state
847 of the biological system, iii) confounding effects of the experimental procedure, such as e.g.
848 stress responses triggered by chemical treatment rather than cell cycle stage, as has been
849 suggested in comparisons of quantitative proteome profiles employing different protocols to
850 achieve cell cycle synchronization (Ly et al., 2015). Further, co-elution may be observed
851 among proteins that participate in physically independent complexes that co-elute in

852 chromatography, as exemplified by NUP50 co-elution with but not participation in the newly
853 identified mitotic NPC sub-complex reported here. Further, experimentally induced
854 disassembly of labile complexes is expectable under SEC-induced dilution and will likely
855 result in an overestimation of the proteins present in monomeric form.

856 Multiple extensions or optimizations of the SEC-SWATH-MS methodology can be
857 envisioned. For example, given the diverse properties of cellular assemblies methodological
858 adaptations could benefit more focused studies of a given complex class of interest, such as
859 e.g. ribosomal complexes (Yoshikawa et al., 2018). Further, limited sample throughput of the
860 method currently precludes time course or cohort analyses (Compare 473 LC-MS
861 measurements and 556 hours of gradient time spent here), a bottleneck which may be
862 bypassed by integrating ultra-fast liquid chromatography setups (Bache et al., 2018) in the
863 SWATH/DIA-MS workflow. Such adaptations will likely render the analysis of proteomes
864 including their organizational state a routine procedure in the near future.

865 Another thrust for further development of the method is bioinformatic information retrieval.
866 We here deliberately chose an approach that makes use of all peptide level information to
867 detect rewiring proteins with maximal sensitivity and at optimal breadth. However, alternative
868 computational strategies can be envisaged that will support the retrieval of additional
869 information from SEC-SWATH-MS data. These include (i) increased sensitivity to detect
870 proteins that exchange interactors without effect on the SEC-SWATH-MS signal (net-0
871 interactome changes) by interaction-network-centered approaches, (ii) improved method
872 throughput by reducing the need for replication and rate of SEC sampling, (iii) improved
873 information retrieval on the level of protein complexes and their precise composition across
874 functional states and (iv) retrieval of information on post-translationally modified and
875 alternatively spliced gene products and the respective impact on complex assembly and
876 dynamics thereof. With developments along those lines ongoing, it appears particularly
877 promising to re-interrogate the SEC-SWATH-MS data presented here from these additional
878 perspectives in the future.

879 In contrast to classical proteomics studies that reduced proteomes to a quantitative list of
880 component parts, SEC-SWATH-MS facilitates studies of the proteome including its
881 biophysical arrangement into complexes as a core functional layer. This enables deep,
882 systems-wide surveys of changes in protein association- and inferred activity states from
883 virtually any experimental system of interest as the method is independent from genetic
884 engineering. The datasets encode protein assembly and interaction states, the composition of
885 complexes and alternate roles of distinct proteoforms. Systematic measurements of protein
886 attributes closely correlated to protein function bear profound potential for the discovery of

887 yet unknown players and mechanisms at the core of (disease) phenotypes generated by
888 biomolecular networks and systems.

889 Acknowledgments

890 We would like to thank the Scientific IT Support (ID SIS) of ETH Zurich for support and
891 maintenance of the Aebersold lab-internal computing infrastructure and the ScopeM facility
892 for continuous support of microscopy at ETH Zurich. The project was supported by the
893 SystemsX.ch projects PhosphoNetX PPM and project TbX to R.A., the Swiss National
894 Science Foundation (grant no. 3100A0-688 107679 to R.A. and 310030_184801 to U.K.), and
895 the European Research Council (ERC-20140AdG 670821 to R.A. and ERC AdG grant
896 NucEnv_322582 to U.K). M.G. acknowledges the support by the Innovative Medicines
897 Initiative project ULTRA-DD (FP07/2007-2013, grant no. 115766). MH was supported by a
898 grant from Institut Mérieux. B.C.C. was supported by a Swiss National Science Foundation
899 Ambizione grant (PZ00P3_161435).

900 Author Contributions

901 Conceived and supervised project, UK, BCC, MG and RA; Performed experiments, MK,
902 SAm, FF and MH, Generated and characterized the HeLa cell line expressing tetracycline-
903 inducible HA-Strep Nup58, MIL, Performed data analysis, MF, MH, SAu; Developed and
904 implemented data analysis tools MF, MH, IB, GR; Writing – original draft, MH; Writing –
905 review & editing, MF, MK, SAm, GR, FF, IB, SAu, BCC, MG, UK, RA.

906 Declaration of Interests

907 The authors declare no conflict of interest.

908

909 Experimental Procedures

910 Cell culture and mitotic arrest

911 HeLa CCL2 cells were obtained from the ATCC collection and cultured in modified complete
912 Dulbecco Modified Eagle Medium (DMEM) at 37°C and 5% CO2. Cells in interphase (early
913 S-phase) were obtained by double-thymidine block. Cells in mitosis (early prometaphase)
914 were obtained by single thymidine block followed by nocodazole treatment and mitotic
915 shake-off, as follows. Cells were grown to a confluency of approximately 60% and arrested in
916 S phase by addition of 3 mM thymidine (Sigma) for 20 h. After overnight incubation the cells
917 were thoroughly washed twice with warm PBS and left for recovery in complete DMEM
918 medium for 2 h prior to addition of 3 mM thymidine (Sigma) and incubation at 37°C for 13 h

919 (interphase-arrest by double thymidine-block), or, for synchronization in mitosis, cells were
920 treated with 100 ng/ml nocodazole at 37°C for 13 h before harvest via mitotic shake-off to
921 ensure recovery of only mitotic cells. Cells arrested in interphase were harvested using
922 EDTA, before cells were pelleted and snap-frozen in liquid nitrogen. Synchronization in
923 interphase and mitosis was confirmed by monitoring phosphorylation of NUP53 by Western
924 blotting and the observed weight gain of mitotic, poly-phosphorylated NUP53 (See **Figure**
925 **3C** and **Figure S1A**).

926 Tandem affinity purification of central channel complexes

927 HeLa cell lines carrying tetracycline-inducible HA-Strep-tagged NUP58 and HA-Strep-
928 tagged GFP were generated using a HeLa Flp-In T-REx cell line (Häfner et al., 2014).
929 Expression of HASt-NUP58 and HASt-GFP were induced by addition of 0.1 µg/mL
930 tetracycline (Sigma). Correct expression and localization of affinity-tagged Nup58 was
931 validated by immunofluorescence and Western blotting (see below). For affinity purifications,
932 bait expression was induced for 48 h before synchronizing the cells in interphase or
933 prometaphase as described above. After washing and pelleting, cells were snap-frozen in
934 liquid nitrogen. Thawed cells were lysed by resuspension in lysis buffer containing 25 mM
935 Tris-HCl pH 7.6, 125 mM NaCl, 2 mM MgCl2, 1 mM DTT, 0.5% NP-40, protease and
936 phosphatase inhibitors and sonicated. After lysate clearance by centrifugation (15'000 rpm, 30
937 min, 4°C), HA-Strep-Nup58 and HA-Strep-GFP were purified by affinity chromatography
938 with StrepTactin sepharose (IBA) for 45 min at 4°C. Beads were washed three times with
939 lysis buffer and one time with lysis buffer without NP40 and protease inhibitors. Bound
940 protein was eluted with elution buffer containing 25 mM Tris-HCl pH 7.6, 125 mM NaCl, 2
941 mM MgCl2, 1 mM DTT and 2.5 mM D-biotin (Sigma). Elutions and input samples were
942 further analysed using SDS-PAGE followed by Western blotting.

943 Western Blotting

944 Cell pellets from synchronized HeLa CCL2 cells and samples from pulldown experiments
945 were resuspended in SDS-sample buffer and briefly denatured at 95°C. Protein was resolved
946 by SDS-PAGE and transferred to nitrocellulose blotting membranes (GE Healthcare).
947 Membranes were blocked over night with 5% skim milk powder in PBS-T (PBS containing
948 0.1% Tween 20). Subsequently, membranes were incubated at RT for 1 h with indicated
949 antibodies diluted in 5% milk-PBS-T. Primary rabbit polyclonal antibodies directed against
950 NUP188, NUP93, NUP53 and NUP54 have been described (Linder et al., 2017). Antibodies
951 directed against actin (Sigma, cat no. A1978), HA (Roche), pH3 (Cell signaling, cat no.
952 9701S) and NUP62 (Abcam, cat no. ab188413) are commercially available. After three
953 washing steps with TBS-T secondary antibody solutions were applied in 5% milk-PBS-T and

954 membranes kept shaking for 1 h at RT. Subsequent washing was followed by detection. HRP-
955 conjugated secondary antibodies used to detect primary antibodies included goat anti–rabbit
956 IgG and goat anti-mouse IgG (Sigma-Aldrich). Chemiluminescence was initiated using ECL
957 detection reagent (GE Healthcare) and the signal was detected using Fuji RX film (Fujifilm)

958 Validation of cell cycle arrest and HASt-NUP58 HeLa cell line by
959 immunofluorescence

960 For immunofluorescence, cells were fixed with 4% paraformaldehyde in PBS, washed with
961 PBS and permeabilized for 5 min in 0.1% Triton X-100. Immunostaining was performed as
962 described previously(Zemp et al., 2009). Briefly, cells were blocked with blocking solution
963 (2% BSA in PBS) at RT for 45 min. Anti-HA antibody (Enzo) was 1:500 diluted and anti-p-
964 Histone H3S10 (Cell Signalling Technology) 1:400 in blocking solution and fixed cells were
965 exposed at RT for 1 hr. Subsequently, cells were washed with blocking solution and stained
966 with fluorescently labelled secondary antibody at a dilution of 1:300. After three washing
967 steps with blocking solution, DNA was stained using Hoechst 33342 (ThermoFisher) 1:5000
968 diluted in blocking solution. Eventually, coverslips were mounted in Vectashield mounting
969 medium (Vector laboratories Inc.) on a glass slide. Localization and expression levels were
970 analysed using a Zeiss LSM 880 upright microscope with a 63x 1.4NA, oil, DIC Plan-
971 Apochromat objective, and Western blotting respectively.

972 Preparation of native proteomes and fractionation for MS analysis

973 Ca. 5e7 HeLa CCL2 cells were mildly lysed by freeze-thawing into 0.5% NP-40 detergent-
974 and protease and phosphatase inhibitor containing buffer, essentially as described(Collins et
975 al., 2013), albeit without the addition of Avidin. Lysates were cleared by 15 minutes of
976 ultracentrifugation (100,000×g, 4 °C) and buffer was exchanged to SEC buffer (50 mM
977 HEPES pH 7.5, 150 mM NaCl) over 30 kDa molecular weight cut-off membrane at a ratio of
978 1:25 and concentrated to 25-35 mg/ml (estimated by OD280). After 5 min of centrifugation at
979 16,900 ×g at 4 °C, the supernatant was directly subjected to fractionation on a SRT-C-SEC
980 500 column (dimensions 300×21.2 mm, pore size 500 Å, particle size 5 µm, Sepax-Tech, DE,
981 USA). Per SEC run, 7.25 mg of native proteome extract (estimated by OD280) was injected
982 and fractionated at 2 ml/min flow rate on ice (0-4 °C), collecting 90 fractions at 0.4 min per
983 fraction from 20 to 56 min post-injection, fractions 1-65 (20 – 46 min elution time, 40 – 92 ml
984 elution volume) of which were considered relevant proteome elution range and considered for
985 quantitative analysis. For library generation purposes, a few fractions from an extended
986 elution range were analyzed (up to fraction 89). In order to minimize time-sensitive artifacts
987 of complex disassembly under dilution, samples were processed independently to achieve a
988 fixed processing time-to-column of 1.5-2 h. Apparent molecular weight per fraction was log-

989 linearly calibrated based on the apex elution fractions of a 5-protein standard sample with
990 known protein mass analyzed with each experimental replicate (Column Performance Check
991 Standard, Aqueous SEC 1, AL0-3042, Phenomenex, CA, USA). An aliquot of the
992 unfractionated mild proteome extract was included in peptide sample preparation and LC-MS
993 analysis.

994 ## MS sample preparation

995 Size exclusion chromatographic fractions and an aliquot of the unfractionated mild proteome
996 extract were processed as follows. Proteins were denatured by the addition of 1% sodium
997 deoxycholate (SDC, Sigma-Aldrich) and heating to 95 °C for 5 min. Disulfide bonds were
998 reduced by adding tris-(2-carboxyethyl)-phosphine to 5 mM and incubating at 37 °C for 30
999 min. Subsequent alkylation of free thiol groups was carried out by adding iodoacetamide to 10
1000 mM and incubating in the dark for 30 min. Proteins were digested by 1.4 µg sequencing grade
1001 trypsin (Promega) per fraction at 37 °C overnight. 1% TFA and 1% ACN were added for
1002 stopping the digestion and precipitating SDC. Additionally, 0.4 pmol of E. coli β-
1003 galactosidase digest were added as internal standard, followed by centrifugation at 4,500 ×g
1004 for 15 min. Subsequently, samples were desalted by means of C18 reversed phase well plates
1005 (96-Well MACROSpin Plate, The Nest Group, MA, USA) according to the manufacturer's
1006 recommendations and vacuum dried. For MS analysis, de-salted peptide samples were re-
1007 suspended in 20 µl LC solvent A (2% ACN, 0.1% FA) supplemented with internal retention
1008 time calibration peptides (iRT kit, Ki-3002-1, Biognosys AG, CH, used at 1:20 instead of
1009 1:10 ratio as indicated in the manufacturer's protocol).

1010 Tandem affinity purified samples were processed as follows. To remove biotin, proteins were
1011 precipitated from the AP eluate by 25% TCA at -20°C overnight and protein pellets were
1012 washed three times with ice-cold acetone and dried. Proteins were denatured by dissolution in
1013 30 µl of 8M urea in 100 mM NH_4HCO_3 at RT, followed by dilution to 0.8 M urea, reduction
1014 by 5 mM TCEP (37°C, 30 min) and alkylation (10 mM iodoacetamide in 100 mM NH_4HCO_3,
1015 37°C, 30 min in the dark) before overnight digestion by sequencing grade trypsin (1 µg,
1016 Promega, 37°C). After adjustment of sample pH to ~2 (using 5% TFA), peptides were de-
1017 salted on C-18 spin columns (3-30 µg capacity, The Nest group) using 0.1% TFA as acidifier
1018 in 2%/50% ACN for washing/elution. For MS measurements, peptides were dissolved in 20
1019 µl 2% ACN. 0.1% FA.

1020 ## LC-MS measurements

1021 Mass spectrometric analysis of the peptide samples generated from the chromatographic
1022 fractions was carried out on an Eksigent nanoLC Ultra 1D Plus and expert 400 autosampler
1023 system (Eksigent, Dublin, CA) coupled to a TripleTOF 6600 (Sciex, Ontario, Canada)

1024 equipped with a NanoSpray III ion source. The acquisition software was Analyst TF 1.7.1. A
1025 75 um inner diameter PicoFrit emitter (New Objective, Woburn, MA) was packed in-house
1026 with Magic C18 AQ 3 um, 200 Å particles (Bruker, Billerica, MA) to a length of 40 cm. It
1027 was operated at a flow of 300 nl/min and at room temperature. The LC solvent A was
1028 composed of 98% ultra-high quality water, 2% acetonitrile and 0.1% formic acid, LC solvent
1029 B was 98% acetonitrile, 2% ultra-high quality water and 0.1% formic acid. 3 µl of sample
1030 were loaded onto the column and separated by a linear gradient from 5 to 35% B in 60 min (or
1031 120 min for DDA and library generation purposes, see below).

1032 For the quantitative analysis of the 390 SEC fractions constituting the core sample set of the
1033 experiment, the TripleTOF was operated in SWATH mode. One MS1 survey scan was
1034 followed by 64 SWATH scans in a looped fashion. The SWATH windows are listed in
1035 Supplementary Table 1, covering precursors in the range of 400-1200 m/z with their widths
1036 chosen to obtain similar precursor intensity densities within all SWATH windows, i.e.
1037 resulting in narrower windows for m/z regions with a high density of precursors. Adjacent
1038 SWATH windows overlapped by 1 m/z to accommodate for the Q1 isolation profile. The
1039 monitored m/z range was 360-1460 in the MS1 scan and 300-2000 in the SWATH scans, the
1040 accumulation time was 200 ms and 50 ms, respectively, which resulted in a cycle time of
1041 around 3.4 s. For fragmentation, a rolling collisional energy (calculated for a theoretical 2+
1042 ion centered in the corresponding SWATH window) with a collisional energy spread of 15 eV
1043 was applied. The ion source was operated with the following settings: spray voltage, 2600 V;
1044 ion source gas flow, 16; curtain gas flow, 35; interface heater temperature, 75°C and
1045 declustering potential, 100.

1046 For the generation of a sample-specific library of peptide query parameters, 83 of the 390 SEC
1047 samples, representing all replicates, elution ranges and conditions and fractions covering an
1048 extended elution range up to F89 in experimental replicate 1, were selected for analysis by data-
1049 dependent acquisition mode over prolonged LCMS gradients of 2 h per sample in order to allow
1050 for deeper coverage of the peptide query parameter library. For DDA runs, samples were
1051 separated by a 120 min linear gradient from 5 to 35% LC solvent B. One MS1 scan was
1052 followed by 20 MS2 scans with an accumulation time of 250 ms for MS1 and 100 ms for MS2.
1053 The monitored m/z range was 360-1460 for MS1 and 50-2000 for MS2. The dynamic exclusion
1054 time was set to 20 s.
1055 AP-MS samples were analyzed by LC-MS/MS on an LTQ-Orbitrap XL system (Thermo
1056 Fisher Scientific) equipped with an EASY nLC II system (Proxeon) operated in DDA mode,
1057 acquiring over an LC gradient of 5-35% of LC solvent B (98% ACN, 0.1% FA) in LC solvent
1058 A (2% ACN, 0.1% FA) in 90 min up to 10 MS/MS spectra of the up to top10 most-abundant

1059 precursors selected from intermittent MS1 survey scans (m/z range, 350-1600 m/z).
1060 Precursors analyzed were dynamically excluded from re-selection for 30 s and with an
1061 exclusion list size of maximally 300 entries. The automatic gain control (AGC) target value
1062 was set to 2e5 for full scans (MS) and 3e4 (MS/MS) scans.

1063 Data processing

1064 DDA-MS data processing

1065 For generation of the peptide query parameter library DDA-MS data acquired in 2 h gradient
1066 time from 83 SEC fractions representative of all replicates, condition and SEC elution ranges
1067 was processed by spectrum-centric analysis and then processed into a spectrum- and reduced
1068 peptide query parameter-library essentially as described(Schubert et al., 2015), except for the
1069 following adaptations: MS spectra were searched for matches to the human UniProt/SwissProt
1070 reference database (reviewed, canonical entries, build: 2017-06-19, supplemented with typical
1071 contaminant (cRAP, https://www.thegpm.org/crap/) and E. coli β-galactosidase sequences)
1072 using trypsin cleavage, 50 ppm precursor and 0.1 Da fragment ion mass tolerance,
1073 carbamidomethyl (C) as static and oxidation (M) as variable modification and allowing up to
1074 two missed cleavages. The results from four independent searches using different search
1075 engines (X!Tandem 2013.06.15.1, Ommsa 2.1.9, MyriMatch 2.1.138 and Comet 2015.02 rev.
1076 3) were integrated using iProphet of the Trans-Proteomic Pipeline ((TPP v4.7 POLAR
1077 VORTEX rev 0, Build 201403121010), filtering the results at 1% peptide FDR (0.978883
1078 iprob) as determined using the tool Mayu(Reiter et al., 2009). We intentionally chose a less
1079 strict peptide-level FDR cut-off (compared to requiring 1% FDR on protein level) in order to
1080 increase sensitivity for the recovery of true positive peptide signals which would be lost as
1081 false negatives under strict protein level FDR control but that can, in an SEC experiment, be
1082 validated by quantitative agreement with high confidence sibling peptides along SEC
1083 fractionation as assessed in downstream data filtering. The spectra were then processed into a
1084 spectral library using the tool Spectrast(Lam et al., 2010) with iRT calibration followed by the
1085 generation of a peptide query parameter library, essentially as described(Schubert et al., 2015)
1086 and within the iPortal compute infrastructure(Kunszt et al., 2015). Query parameters were
1087 composed selecting the 6 most abundant fragment ion transitions per precursor from the b or y
1088 ion series within m/z range 350-2000 and allowing fragment charge states 1-2 and no mass
1089 gains or losses. The final library contains query parameters for 111,267 precursors of 90,932
1090 peptides mapping to 9603 protein groups that were subsequently targeted for quantification in
1091 the 390 60 min gradient SWATH-MS runs of the 390 SEC fractions. Given the strict rules
1092 employed for downstream quantification (quantifying only single, unique proteins with at
1093 least 2 unique, proteotypic peptides) the number of maximally detectable analytes as
1094 constrained by the query parameter library drops to 102,629 precursors of 83,863 peptides

1095 mapping to 5,916 unique proteins. 60 min DDA-MS data were processed equivalently by
1096 spectrum-centric analysis to obtain spectral counts across chromatographic fractions as
1097 quantitative measure for technical comparisons (DDA search results and the spectral and
1098 peptide query parameter libraries are available via ProteomeXchange, see section data
1099 availability below).

1100 ### SWATH-MS data processing

1101 The SWATH -MS data were analyzed via targeted, peptide-centric analysis, querying 111,267
1102 precursors from the sample-specific peptide query parameter library (see above) in the
1103 SWATH fragment ion chromatograms, using a modified OpenSWATH(Röst et al., 2014),
1104 PyProphet (Reiter et al., 2011; Teleman et al., 2015) and TRIC(Röst et al., 2016) workflow.
1105 First, one global classifier was trained on a subsampled set of SEC fractions across the
1106 experiment using pyProphet-cli (Rosenberger et al., 2017) (Specifically, fractions 3, 43 and
1107 44 of each replicate and condition were analyzed jointly in order to generate a stable scoring
1108 function from the most analyte-rich measurements (F43 and F44) while including different
1109 analytes detected exclusively in the high MW range (F3)). Peptides from all fractions were
1110 then quantified and scored using the pre-trained scoring function using OpenSWATH,
1111 pyProphet and TRIC in the iPortal framework(Kunszt et al., 2015). TRIC was set to recover
1112 precursors at an experiment-wide assay/peptide query-level (TRIC target) FDR of 5%. The
1113 full result table (E1709051521_feature_alignment.tsv.gz) has been deposited, together with
1114 the MS raw data, to ProteomeXchange, see section data availability below.

1115 ### Downstream SEC-SWATH-MS data processing and FDR estimation

1116 Precursor-level results from E1709051521_feature_alignment.tsv were imported into
1117 CCprofiler extended by the protein-centric differential analysis module. Upon import,
1118 precursor intensity signals (summed intensity of the 6 most-abundant fragment ion XIC peak
1119 area) were summed per peptide (function: *importFromOpenSWATH*). Then, missing values
1120 flanked by at least two consecutive identifications were imputed by a spline fit (function:
1121 *findMissingValues*).Traces were scaled to the internal standard spike-in peptides of E. coli β-
1122 galactosidase (P00722, function: *normalizeToStandard*) followed by smoothing of total
1123 intensities according to a spline fit over total MS intensity sums (function: *smootheTraces*).
1124 The data were further filtered on chromatography-informed scores following final FDR
1125 estimation based on the simple target-decoy method. Specific filtering rules were, first,
1126 eliminating all values part of consecutive identification stretches below length three and,
1127 second, exclusion of peptides based on their quantitative fractionation pattern's average
1128 dissimilarity to those of sibling peptides (originating from the same parent protein). Guided
1129 by the fraction of decoys remaining (target: 3% on unique protein identifier level), peptides

1130 with average sibling peptide correlation coefficient (spc) below [0.28 - 0.34] were removed,
1131 with cut-offs selected to achieve a decoy rate below 3% among the remaining protein entries.
1132 Subsequently, proteins were quantified by summing the top2 most-intense peptide signals.
1133 Protein intensity across the replicates was averaged and standard errors of the mean
1134 calculated. Cumulatively, 5044 proteins were characterized. The FDR on protein level was
1135 estimated based on the simple target-decoy method, with correction for the fraction of false
1136 protein targets (equivalent to the fraction of absent proteins, π_A(The et al., 2016)). We
1137 estimate π_A as the fraction of library-contained target proteins that were not detected with
1138 high confidence in the targeted analysis, i.e. $\pi_A \approx (5{,}916 - 5{,}044) / 5{,}916 = 0.147$. This
1139 estimation is conservative because not all true positive proteins are recovered at high
1140 confidence, leading to overestimation of π_A and thus more conservative corrected FDR
1141 estimates. Accordingly, 135 decoy entries passing the filters together with the 5044 target
1142 proteins (decoy rate, 0.026) point to an estimated global protein level FDR of (135 * 0.147) /
1143 5,044 = 0.0039, ≤ 0.4%.

1144 ### Protein-centric differential SEC distribution testing

1145 To detect proteins that significantly alter their quantitative SEC elution pattern we devised a
1146 protein-centric differential analysis pipeline that leverages all information on peptide level to
1147 identify proteins that shift elution behavior across distinct SEC ranges of elution (elution
1148 features). First, the global set of protein elution features apparent from the dataset were
1149 detected from an integrated set of peptide chromatograms (traces) using the SECprofiler
1150 framework, followed by statistical testing for differences based on the intensities observed in
1151 the different experimental replicates. Specifically, peptide traces were averaged within the
1152 conditions and then artificially combined into one summed set of 60891 traces (function
1153 *integrateTraceIntensities*). Then, high confidence protein elution features were detected as
1154 signals of co-peaking peptide traces, grouping the traces by parent protein identifier and
1155 including decoys with randomized peptide-to-protein mapping (functions:
1156 *findProteinFeatures*, *calculateCoelutionScore* and *calculateQvalue*). At a q-value cut-off of
1157 5%, 6044 protein elution features were detected to define the ranges for differential
1158 abundance tests.

1159 To detect differential SEC elution behavior, peptide abundances in the elution ranges were
1160 then tested for significant differences in abundance, using the functions *extractFeatureVals*
1161 and *testDifferentialExpression* and employing the paired t-test as statistical metric. All tests
1162 were based on the raw variability of the data, i.e. minimally processed data points (essentially,
1163 only scaled within conditions), to avoid biases introduced by data processing. Missing values
1164 were replaced by uniformly sampled intensities in the 5th percentile of quantified values. The
1165 test results were collected on protein level by deriving a fold-change adjusted median p-value

1166 from all peptide tests mapping to the respective parent proteins (Suomi and Elo, 2017). Using
1167 the function *aggregatePeptideTests* the protein level significance was calculated using a
1168 cumulative beta distribution parametrized on the number observed of peptides (Suomi and
1169 Elo, 2017). This resulted in protein p-values for 1-5 individual features per protein with
1170 separate scoring. To simplify visualization and reduce the results to one set of scores per
1171 protein, for each protein the lowest pBHadj and largest fold-change of which was selected for
1172 visualization in the screen hit volcano plot (See **Figure 1 D**). The R package *CCprofiler*,
1173 extended by the protein-centric differential analysis module is available via GitHub
1174 (https://github.com/CCprofiler/CCprofiler/tree/helaCC).

1175 ### AP-MS data analysis

1176 AP-MS DDA-MS data were analyzed by spectrum-centric analysis matching spectra against
1177 the human reviewed SwissProt reference sequence database (build 2018-08-01) using three
1178 search engines (X!Tandem, Myrimatch and Comet) and result integration via the Trans-
1179 proteomic pipeline (TPP), applying FDR cut-offs of 1% at the peptide level (iprophet-
1180 pepFDR, ≥ 0.6581 iprobability) and protein level (ProteinProphet), executed within the iportal
1181 framework (Kunszt et al., 2015). Searches allowed mass tolerances of 15 ppm and 0.4 Da on
1182 precursor and fragment ion level. Enzyme specificity was set to Trypsin, allowing up to two
1183 missed cleavages. Carbamidomethyl was set as static modification, no variable modifications
1184 were considered.

1185 ### Assignment of Nuclear pore complex components

1186 Nuclear pore complex members were assigned based on two consecutively applied criteria, i)
1187 Uniprot query (nuclear pore complex AND reviewed:yes AND organism:"Homo sapiens
1188 (Human) [9606]") and ii) structural assignment in Table 1 by Hoelz et al. (Hoelz et al., 2016),
1189 resulting in 32 canonical subunits employed for benchmarking and exploration of NPC
1190 disassembly sub-complexes.

1191 ## Data availability

1192 The mass spectrometry proteomics raw data and processing results have been deposited to the
1193 ProteomeXchange Consortium (http://proteomecentral.proteomexchange.org) via the PRIDE
1194 partner repository(Vizcaíno et al., 2012) with the dataset identifier PXD010288. The data are
1195 available in easily browsable and searchable form via https://sec-
1196 explorer.shinyapps.io/hela_cellcycle/. The full dataset can be accessed using the password
1197 "ethsecexplorer".

1198 # List of Figures

1199 The manuscript contains the following figures.

1200 Figure 1: Proteome rearrangement screening by SEC-SWATH-MS: Workflow and dataset
1201 properties.

1202 Figure 2: Proteome rearrangement screening by SEC-SWATH-MS: Data acquisition and
1203 processing.

1204 Figure 3: Benchmarking part 1: Recall of expected mitotic complex remodeling events.

1205 Figure 4: Benchmarking part 2: Performance of measuring proteome state dynamics by
1206 apparent size vs. thermostability.

1207 Figure 5: Inference of cell-cycle dependent complex remodeling.

1208 Figure 6: Discovery and independent validation of NPC disassembly intermediates.

1209 Figure 7: Browsing dynamic complex association maps in SECexplorer-cc.

1210 Supplemental Figures S1-6 are provided with the Supplemental Information.

1211 Supplemental Information

1212 The supplemental information Supplemental Figures (S1-S6). Further, one Supplemental Item
1213 (SI1) and three Supplemental Tables (ST1-3) with self-contained legends where applicable
1214 are provided with the following titles.

1215 Supplemental Figure S1: Validation of homogenous cell cycle arrest and of inducible Nup58-
1216 expressing HeLa cell lines

1217 Supplemental Figure S2: Benchmarking the SEC-SWATH-MS workflow - correction of
1218 longitudinal effects and replicate intensity correlation

1219 Supplemental Figure S3: Pathway enrichment among top 1000 proteins recovered by size or
1220 thermostability profiling along the cell cycle

1221 Supplemental Figure S4: Protein elution peak detection and properties of multi-complex
1222 signal proteins

1223 Supplemental Figure S5: Investigation of RAP1-TRF2-IKK cross-complex interaction and
1224 zoom-in to NUP93 subpopulations resolved across mitotic states

1225 Supplemental Figure S6: Investigation of SEC13 moonlighting across Nup107-160
1226 subcomplex and COPII vesicle transport related complexes.

1227 Supplemental Item SI1: SEC-SWATH-MS protein chromatogram plots

1228 Supplemental Table ST1: Global protein quantification summary table

1229 Supplemental Table ST2: Global protein elution peak detection and statistical scoring
1230 summary table

1231 Supplemental Table ST3: Global complex remodeling summary table

1232 References

1233 Aebersold, R., and Mann, M. (2016). Mass-spectrometric exploration of proteome structure
1234 and function. Nature *537*, 347–355.

1235 Arat, N.Ö., and Griffith, J.D. (2012). Human Rap1 Interacts Directly with Telomeric DNA
1236 and Regulates TRF2 Localization at the Telomere. J. Biol. Chem. *287*, 41583–41594.

1237 Bache, N., Geyer, P.E., Bekker-Jensen, D.B., Hoerning, O., Falkenby, L., Treit, P. V, Doll, S.,
1238 Paron, I., Müller, J.B., Meier, F., et al. (2018). A Novel LC System Embeds Analytes in Pre-
1239 formed Gradients for Rapid, Ultra-robust Proteomics. Mol. Cell. Proteomics *17*, 2284–2296.

1240 Becher, I., Andrés-Pons, A., Romanov, N., Stein, F., Schramm, M., Baudin, F., Helm, D.,
1241 Kurzawa, N., Mateus, A., Mackmull, M.T., et al. (2018). Pervasive Protein Thermal Stability
1242 Variation during the Cell Cycle. Cell *173*, 1495-1507.e18.

1243 Beck, M., and Hurt, E. (2017). The nuclear pore complex: understanding its function through
1244 structural insight. Nat. Rev. Mol. Cell Biol. *18*, 73–89.

1245 Chug, H., Trakhanov, S., Hülsmann, B.B., Pleiner, T., and Görlich, D. (2015). Crystal
1246 structure of the metazoan Nup62•Nup58•Nup54 nucleoporin complex. Science (80). *350*,
1247 106–110.

1248 Collins, B.C., Gillet, L.C., Rosenberger, G., Röst, H.L., Vichalkovski, A., Gstaiger, M., and
1249 Aebersold, R. (2013). Quantifying protein interaction dynamics by SWATH mass
1250 spectrometry: application to the 14-3-3 system. Nat. Methods *10*, 1246–1253.

1251 Collins, B.C., Hunter, C.L., Liu, Y., Schilling, B., Rosenberger, G., Bader, S.L., Chan, D.W.,
1252 Gibson, B.W., Gingras, A.-C., Held, J.M., et al. (2017). Multi-laboratory assessment of
1253 reproducibility, qualitative and quantitative performance of SWATH-mass spectrometry. Nat.
1254 Commun. *8*, 291.

1255 Dai, L., Zhao, T., Bisteau, X., Sun, W., Prabhu, N., Lim, Y.T., Sobota, R.M., Kaldis, P., and
1256 Nordlund, P. (2018). Modulation of Protein-Interaction States through the Cell Cycle. Cell
1257 *173*, 1481-1494.e13.

1258 Dominguez, D., Tsai, Y.-H., Weatheritt, R., Wang, Y., Blencowe, B.J., Wang, Z., Matese, J.,
1259 Perou, C., Hurt, M., Brown, P., et al. (2016). An extensive program of periodic alternative
1260 splicing linked to cell cycle progression. Elife *5*, 191–207.

1261 Dong, M., Yang, L.L., Williams, K., Fisher, S.J., Hall, S.C., Biggin, M.D., Jin, J., and
1262 Witkowska, H.E. (2008). A "tagless" strategy for identification of stable protein complexes
1263 genome-wide by multidimensional orthogonal chromatographic separation and iTRAQ
1264 reagent tracking. J. Proteome Res. *7*, 1836–1849.

1265 Dunkley, T.P.J., Watson, R., Griffin, J.L., Dupree, P., and Lilley, K.S. (2004). Localization of
1266 organelle proteins by isotope tagging (LOPIT). Mol. Cell. Proteomics *3*, 1128–1134.

1267 Foster, L.J., de Hoog, C.L., Zhang, Y., Zhang, Y., Xie, X., Mootha, V.K., and Mann, M.
1268 (2006). A mammalian organelle map by protein correlation profiling. Cell *125*, 187–199.

1269 Gavet, O., and Pines, J. (2010). Activation of cyclin B1–Cdk1 synchronizes events in the
1270 nucleus and the cytoplasm at mitosis. J. Cell Biol. *189*, 247–259.

1271 Gillet, L.C., Navarro, P., Tate, S., Röst, H., Selevsek, N., Reiter, L., Bonner, R., and
1272 Aebersold, R. (2012). Targeted data extraction of the MS/MS spectra generated by data-
1273 independent acquisition: a new concept for consistent and accurate proteome analysis. Mol.
1274 Cell. Proteomics *11*, O111.016717.

1275 Gillet, L.C., Leitner, A., and Aebersold, R. (2016). Mass Spectrometry Applied to Bottom-Up
1276 Proteomics: Entering the High-Throughput Era for Hypothesis Testing. Annu. Rev. Anal.
1277 Chem. *9*, 449–472.

1278 Gong, D., Pomerening, J.R., Myers, J.W., Gustavsson, C., Jones, J.T., Hahn, A.T., Meyer, T.,
1279 and Ferrell Jr., J.E. (2007). Cyclin A2 Regulates Nuclear-Envelope Breakdown and the
1280 Nuclear Accumulation of Cyclin B1. Curr. Biol. *17*, 85–91.

1281 Häfner, J., Mayr, M.I., Möckel, M.M., and Mayer, T.U. (2014). Pre-anaphase chromosome
1282 oscillations are regulated by the antagonistic activities of Cdk1 and PP1 on Kif18A. Nat.
1283 Commun. *5*, 4397.

1284 Hartwell, L.H., Hopfield, J.J., Leibler, S., and Murray, A.W. (1999). From molecular to
1285 modular cell biology. Nature *402*, C47-52.

1286 Heusel, M., Bludau, I., Rosenberger, G., Hafen, R., Frank, M., Banaei-Esfahani, A., Drogen,
1287 A. van, Collins, B.C., Gstaiger, M., and Aebersold, R. (2019). Complex-centric proteome
1288 profiling by SEC-SWATH-MS. Mol. Syst. Biol. *15*, e8438.

1289 Hoelz, A., Glavy, J.S., and Beck, M. (2016). Toward the atomic structure of the nuclear pore
1290 complex: when top down meets bottom up. Nat. Struct. Mol. Biol. *23*, 624–630.

1291 Ideker, T., Galitski, T., and Hood, L. (2001). A new approach to decoding life: systems
1292 biology. Annu. Rev. Genomics Hum. Genet. *2*, 343–372.

1293 Itzhak, D.N., Tyanova, S., Cox, J., and Borner, G.H. (2016). Global, quantitative and dynamic
1294 mapping of protein subcellular localization. Elife *5*.

1295 Kristensen, A.R., Gsponer, J., and Foster, L.J. (2012). A high-throughput approach for
1296 measuring temporal changes in the interactome. Nat. Methods *9*, 907–909.

1297 Kunszt, P., Blum, L., Hullár, B., Schmid, E., Srebniak, A., Wolski, W., Rinn, B., Elmer, F.-J.,
1298 Ramakrishnan, C., Quandt, A., et al. (2015). iPortal: the swiss grid proteomics portal:
1299 Requirements and new features based on experience and usability considerations. Concurr.
1300 Comput. Pract. Exp. *27*, 433–445.

1301 Lam, H., Deutsch, E.W., and Aebersold, R. (2010). Artificial decoy spectral libraries for false
1302 discovery rate estimation in spectral library searching in proteomics. J. Proteome Res. *9*, 605–
1303 610.

1304 Larance, M., Kirkwood, K.J., Tinti, M., Brenes Murillo, A., Ferguson, M.A.J., and Lamond,
1305 A.I. (2016). Global Membrane Protein Interactome Analysis using *In vivo* Crosslinking and
1306 Mass Spectrometry-based Protein Correlation Profiling. Mol. Cell. Proteomics *15*, 2476–
1307 2490.

1308 Laurell, E., Beck, K., Krupina, K., Theerthagiri, G., Bodenmiller, B., Horvath, P., Aebersold,
1309 R., Antonin, W., and Kutay, U. (2011). Phosphorylation of Nup98 by Multiple Kinases Is
1310 Crucial for NPC Disassembly during Mitotic Entry. Cell *144*, 539–550.

1311 Leuenberger, P., Ganscha, S., Kahraman, A., Cappelletti, V., Boersema, P.J., von Mering, C.,
1312 Claassen, M., and Picotti, P. (2017). Cell-wide analysis of protein thermal unfolding reveals
1313 determinants of thermostability. Science (80-.). *355*, eaai7825.

1314 Lin, D.H., Stuwe, T., Schilbach, S., Rundlet, E.J., Perriches, T., Mobbs, G., Fan, Y.,
1315 Thierbach, K., Huber, F.M., Collins, L.N., et al. (2016). Architecture of the symmetric core of
1316 the nuclear pore. Science (80-.). *352*, aaf1015–aaf1015.

1317 Linder, M.I., Köhler, M., Boersema, P., Weberruss, M., Wandke, C., Marino, J., Ashiono, C.,
1318 Picotti, P., Antonin, W., and Kutay, U. (2017). Mitotic Disassembly of Nuclear Pore
1319 Complexes Involves CDK1- and PLK1-Mediated Phosphorylation of Key Interconnecting
1320 Nucleoporins. Dev. Cell *43*, 141-156.e7.

1321 Liu, F., and Fitzgerald, M.C. (2016). Large-Scale Analysis of Breast Cancer-Related
1322 Conformational Changes in Proteins Using Limited Proteolysis. J. Proteome Res. *15*, 4666–
1323 4674.

1324 Liu, D., Safari, A., O'Connor, M.S., Chan, D.W., Laegeler, A., Qin, J., and Songyang, Z.
1325 (2004). PTOP interacts with POT1 and regulates its localization to telomeres. Nat. Cell Biol.
1326 *6*, 673–680.

1327 Liu, X., Yang, W., Gao, Q., and Regnier, F. (2008). Toward chromatographic analysis of
1328 interacting protein networks. J. Chromatogr. A *1178*, 24–32.

1329 Ludwig, C., and Aebersold, R. Getting Absolute : Determining Absolute Protein Quantities
1330 via Selected Reaction Monitoring Mass Spectrometry. 80–109.

1331 Ly, T., Endo, A., and Lamond, A.I. (2015). Proteomic analysis of the response to cell cycle
1332 arrests in human myeloid leukemia cells. Elife *4*.

1333 Nigg, E.A. (1993). Cellular substrates of p34(cdc2) and its companion cyclin-dependent
1334 kinases. Trends Cell Biol. *3*, 296–301.

1335 Peyressatre, M., Prével, C., Pellerano, M., and Morris, M.C. (2015). Targeting cyclin-
1336 dependent kinases in human cancers: from small molecules to Peptide inhibitors. Cancers
1337 (Basel). *7*, 179–237.

1338 Reiter, L., Claassen, M., Schrimpf, S.P., Jovanovic, M., Schmidt, A., Buhmann, J.M.,
1339 Hengartner, M.O., and Aebersold, R. (2009). Protein identification false discovery rates for
1340 very large proteomics data sets generated by tandem mass spectrometry. Mol. Cell.
1341 Proteomics *8*, 2405–2417.

1342 Reiter, L., Rinner, O., Picotti, P., Hüttenhain, R., Beck, M., Brusniak, M.-Y., Hengartner,
1343 M.O., and Aebersold, R. (2011). mProphet: automated data processing and statistical
1344 validation for large-scale SRM experiments. Nat. Methods *8*, 430–435.

1345 Rosenberger, G., Ludwig, C., Röst, H.L., Aebersold, R., and Malmström, L. (2014). aLFQ: an
1346 R-package for estimating absolute protein quantities from label-free LC-MS/MS proteomics
1347 data. Bioinformatics *30*, 2511–2513.

1348 Rosenberger, G., Bludau, I., Schmitt, U., Heusel, M., Hunter, C.L., Liu, Y., MacCoss, M.J.,
1349 MacLean, B.X., Nesvizhskii, A.I., Pedrioli, P.G.A., et al. (2017). Statistical control of peptide
1350 and protein error rates in large-scale targeted data-independent acquisition analyses. Nat.
1351 Methods *14*, 921–927.

1352 Röst, H.L., Rosenberger, G., Navarro, P., Gillet, L., Miladinović, S.M., Schubert, O.T.,
1353 Wolski, W., Collins, B.C., Malmström, J., Malmström, L., et al. (2014). OpenSWATH

1354 enables automated, targeted analysis of data-independent acquisition MS data. Nat.
1355 Biotechnol. *32*, 219–223.

1356 Röst, H.L., Liu, Y., D'Agostino, G., Zanella, M., Navarro, P., Rosenberger, G., Collins, B.C.,
1357 Gillet, L., Testa, G., Malmström, L., et al. (2016). TRIC: an automated alignment strategy for
1358 reproducible protein quantification in targeted proteomics. Nat. Methods *13*, 777–783.

1359 Ruepp, A., Waegele, B., Lechner, M., Brauner, B., Dunger-Kaltenbach, I., Fobo, G.,
1360 Frishman, G., Montrone, C., and Mewes, H.-W. (2010). CORUM: the comprehensive
1361 resource of mammalian protein complexes--2009. Nucleic Acids Res. *38*, D497-501.

1362 Schopper, S., Kahraman, A., Leuenberger, P., Feng, Y., Piazza, I., Müller, O., Boersema, P.J.,
1363 and Picotti, P. (2017). Measuring protein structural changes on a proteome-wide scale using
1364 limited proteolysis-coupled mass spectrometry. Nat. Protoc. *12*, 2391–2410.

1365 Schubert, O.T., Gillet, L.C., Collins, B.C., Navarro, P., Rosenberger, G., Wolski, W.E., Lam,
1366 H., Amodei, D., Mallick, P., MacLean, B., et al. (2015). Building high-quality assay libraries
1367 for targeted analysis of SWATH MS data. Nat. Protoc. *10*, 426–441.

1368 Scott, N.E., Rogers, L.D., Prudova, A., Brown, N.F., Fortelny, N., Overall, C.M., and Foster,
1369 L.J. (2017). Interactome disassembly during apoptosis occurs independent of caspase
1370 cleavage. Mol. Syst. Biol. *13*, 906.

1371 Stacey, R.G., Skinnider, M.A., Scott, N.E., and Foster, L.J. (2017). A rapid and accurate
1372 approach for prediction of interactomes from co-elution data (PrInCE). BioRxiv 152355.

1373 Suomi, T., and Elo, L.L. (2017). Enhanced differential expression statistics for data-
1374 independent acquisition proteomics. Sci. Rep. *7*, 5869.

1375 Szklarczyk, D., Morris, J.H., Cook, H., Kuhn, M., Wyder, S., Simonovic, M., Santos, A.,
1376 Doncheva, N.T., Roth, A., Bork, P., et al. (2017). The STRING database in 2017: quality-
1377 controlled protein–protein association networks, made broadly accessible. Nucleic Acids Res.
1378 *45*, D362–D368.

1379 Tan, C.S.H., Go, K.D., Bisteau, X., Dai, L., Yong, C.H., Prabhu, N., Ozturk, M.B., Lim, Y.T.,
1380 Sreekumar, L., Lengqvist, J., et al. (2018). Thermal proximity coaggregation for system-wide
1381 profiling of protein complex dynamics in cells. Science *359*, 1170–1177.

1382 Tang, B.L., Peter, F., Krijnse-Locker, J., Low, S.H., Griffiths, G., and Hong, W. (1997). The
1383 mammalian homolog of yeast Sec13p is enriched in the intermediate compartment and is
1384 essential for protein transport from the endoplasmic reticulum to the Golgi apparatus. Mol.
1385 Cell. Biol. *17*, 256–266.

1386 Teleman, J., Röst, H.L., Rosenberger, G., Schmitt, U., Malmström, L., Malmström, J., and
1387 Levander, F. (2015). DIANA--algorithmic improvements for analysis of data-independent
1388 acquisition MS data. Bioinformatics *31*, 555–562.

1389 Teo, H., Ghosh, S., Luesch, H., Ghosh, A., Wong, E.T., Malik, N., Orth, A., de Jesus, P.,
1390 Perry, A.S., Oliver, J.D., et al. (2010). Telomere-independent Rap1 is an IKK adaptor and
1391 regulates NF-κB-dependent gene expression. Nat. Cell Biol. *12*, 758–767.

1392 The, M., Tasnim, A., and Käll, L. (2016). How to talk about protein-level false discovery
1393 rates in shotgun proteomics. Proteomics *16*, 2461–2469.

1394 Vermeulen, K., Van Bockstaele, D.R., and Berneman, Z.N. (2003). The cell cycle: a review of
1395 regulation, deregulation and therapeutic targets in cancer. Cell Prolif. *36*, 131–149.

1396 Vizcaíno, J.A., Côté, R.G., Csordas, A., Dianes, J.A., Fabregat, A., Foster, J.M., Griss, J.,
1397 Alpi, E., Birim, M., Contell, J., et al. (2012). The Proteomics Identifications (PRIDE)
1398 database and associated tools: status in 2013. Nucleic Acids Res. *41*, D1063–D1069.

1399 Wan, C., Borgeson, B., Phanse, S., Tu, F., Drew, K., Clark, G., Xiong, X., Kagan, O., Kwan,
1400 J., Bezginov, A., et al. (2015). Panorama of ancient metazoan macromolecular complexes.
1401 Nature.

1402 Wessels, H.J.C.T., Vogel, R.O., van den Heuvel, L., Smeitink, J.A., Rodenburg, R.J.,
1403 Nijtmans, L.G., and Farhoud, M.H. (2009). LC-MS/MS as an alternative for SDS-PAGE in
1404 blue native analysis of protein complexes. Proteomics *9*, 4221–4228.

1405 Xu, Y., Strickland, E.C., and Fitzgerald, M.C. (2014). Thermodynamic Analysis of Protein
1406 Folding and Stability Using a Tryptophan Modification Protocol. Anal. Chem. *86*, 7041–
1407 7048.

1408 Yoshikawa, H., Larance, M., Harney, D.J., Sundaramoorthy, R., Ly, T., Owen-Hughes, T.,
1409 and Lamond, A.I. (2018). Efficient analysis of mammalian polysomes in cells and tissues
1410 using Ribo Mega-SEC. Elife *7*.

1411 Zemp, I., Wild, T., O'Donohue, M.-F., Wandrey, F., Widmann, B., Gleizes, P.-E., and Kutay,
1412 U. (2009). Distinct cytoplasmic maturation steps of 40S ribosomal subunit precursors require
1413 hRio2. J. Cell Biol. *185*, 1167–1180.